

Unprecedented flow strength in shock-compressed nano-polycrystalline diamond

Anirudh Hari^{1,2,3,23}, Kento Katagiri^{1,2,3,4,5,23*}, Wanghui Li^{6,23}, Dorian P. Luccioni^{1,2,3}, Rayen Lin^{1,3,7}, Sophie E. Parsons^{1,2,3}, Rohit Hari⁸, Tharun Reddy^{1,2,3}, Ernest W. Cubit II^{1,2,3}, Alexis Amouretti⁴, Jon H. Eggert⁹, Yuichi Inubushi^{10,11}, Tetsuo Irifune^{12,13}, Sara J. Irvine^{2,3,14}, Ryosuke Kodama^{4,5}, Michel Koenig^{4,15}, Laura Madril^{1,2,3}, Takeshi Matsuoka¹⁶, Kohei Miyanishi¹¹, Hirotaka Nakamura⁴, Norimasa Nishiyama¹⁷, Takuo Okuchi¹⁸, Masato Ota¹⁹, Toshimori Sekine^{4,20}, Yusuke Seto²¹, Toru Shinmei¹², Keiichi Sueda¹¹, Yoshinori Tange¹⁰, Sota Takagi²², Tadashi Togashi^{10,11}, Yuhei Umeda¹⁸, Yifan Wang^{1,2,3}, Makina Yabashi^{10,11}, Toshinori Yabuuchi^{10,11}, Norimasa Ozaki^{4,5}, and Leora E. Dresselhaus-Marais^{1,2,3*}

¹Stanford University, Department of Materials Science and Engineering, California 94305, USA

²SLAC National Accelerator Laboratory, California 94025, USA

³Stanford University, PULSE Institute, California 94305, USA

⁴Graduate School of Engineering, Osaka University, Osaka 565-0871, Japan

⁵Institute of Laser Engineering, Osaka University, Osaka 565-0871, Japan

⁶Institute of High Performance Computing (IHPC), Agency for Science, Technology and Research (A*STAR), Singapore 138632, Republic of Singapore

⁷University of California, Los Angeles, Department of Materials Science and Engineering, California 90095, USA

⁸Georgia Institute of Technology, Department of Electrical and Computer Engineering, Georgia 30332, USA

⁹Lawrence Livermore National Laboratory, California 94550, USA

¹⁰Japan Synchrotron Radiation Research Institute, Hyogo 679-5198, Japan

¹¹RIKEN SPring-8 Center, Hyogo 679-5148, Japan

¹²Geodynamics Research Center, Ehime University, Ehime 790-0826, Japan

¹³Earth-Life Science Institute, Tokyo Institute of Technology, Tokyo 145-0061, Japan

¹⁴Stanford University, Department of Applied Physics, California 94305, USA

¹⁵LULI, CNRS, CEA, École Polytechnique, UPMC, Univ Paris 06: Sorbonne Universités, Institut Polytechnique de Paris, 91128 Palaiseau cedex, France

¹⁶Open and Transdisciplinary Research Initiatives, Osaka University, Osaka 565-0871, Japan

¹⁷Laboratory for Materials and Structures, Tokyo Institute of Technology, Kanagawa 226-8503, Japan

¹⁸Institute for Integrated Radiation and Nuclear Science, Kyoto University; Osaka 590-0494, Japan

¹⁹National Institute for Fusion Science, Gifu, Japan

²⁰Center for High-Pressure Science and Technology Advanced Research, Shanghai 201203, China

²¹Graduate School of Science, Kobe University; Hyogo 657-0013, Japan

²²Earth and Planets Laboratory, Carnegie Institution for Science, Washington DC 20015, USA

²³These authors contributed equally to this work.

Correspondence: kentok@stanford.edu, leoradm@stanford.edu

Diamond is the hardest natural material and thus offers unique insights into materials design [1-3]. Extreme pressures and temperatures create conditions that allow even strong and brittle materials like diamond to deform plastically and exhibit flow strength, i.e., resistance to plastic flow [4-6]. Despite significant research, the upper limit of flow strength in diamond materials under high energy conditions remains uncertain, and the mechanisms driving the deformation are a subject of intense debate [7–11]. Here, we demonstrate that stacking-fault mediated strengthening enables nano-polycrystalline diamond (NPD) to achieve a peak flow strength of 107 ± 5 GPa. Achieved through shock loading to multi-megabar stresses, this unprecedented flow strength represents a five-fold increase compared to that of quasi-statically compressed NPD [6]. Our femtosecond *in situ* X-ray diffraction (XRD) experiments and large-scale molecular dynamics simulations probe this phenomenon mechanistically. Our work shows that by subjecting materials to the most extreme conditions, we can unlock unusual strength and mechanical properties.

Diamond exhibits unique mechanical properties and high thermal conductivity owing to its tetrahedral covalent bonding and lack of close-packed planes [12]. The Knoop hardness of single-crystal diamond varies from 60–120 GPa, depending on its crystallographic orientation [13]. Microstructural advances have utilized nano-grain and nano-twin boundaries to significantly increase diamond's hardness up to 140–200 GPa and its fracture toughness up to $15 \text{ MPa m}^{1/2}$ [1–3]. This hardening has been attributed to Hall-Petch strengthening [3] as well as lamellar grain structures deflecting crack propagation [2]. Under ambient conditions, diamond fractures when stressed beyond its elastic limit. However, extreme pressures and temperatures suppress cracking, allowing even brittle materials like diamond to deform plastically [4–6]. Under such conditions,

the resistance to plastic deformation (flow strength) is the key parameter governing the mechanical response [14].

Shock loading is a widely used and effective way to generate ultrahigh, multi-megabar pressure conditions. In metals under shock compression, the flow strength is governed by dislocation-mediated slip and twinning [15,16]. By contrast, diamond has been historically regarded as inherently brittle, so most shock-wave studies focus on its elastic limit [8,9,17,18]. How high the flow strength can reach and what plastic deformation mechanisms become active in diamond under shock compression remain unclear. Recent imaging experiments of shocked single crystal diamond revealed linear features along the {111} planes that were attributed to stacking faults bound by partial dislocations [11], but this interpretation is still under debate. It remains unclear what the nature of these shock-specific deformation mechanisms are, and how they contribute to diamond's mechanical properties. Regarding the flow strength, one study attempted to probe the flow strength of shocked single-crystalline diamond via velocimetry, but large uncertainties in their measurements and models make it difficult to interpret the data [7]. Another study used *in situ* XRD to probe the flow strength of shocked micro-polycrystalline diamond and found some evidence of strength, but a small sampling of diffracting grains similarly led to large uncertainties that make it difficult to observe any trends [10]. As a result, both the flow strength and its associated deformation mechanisms in shocked diamond are largely unknown. This presents challenges in designing stronger materials for use in extreme environments.

To reveal the limits of diamond's strength and its mechanisms, we use full-density nano-polycrystalline diamond (NPD) as a model system. NPD has a Knoop hardness of up to 140 GPa, and under quasi-static compression, it reaches an ultimate strength of up to 22 GPa [6], making it an ideal material to study novel strengthening behavior under shock. We probed the flow strength

of NPD under laser-driven shock compression, with femtosecond *in situ* XRD at the SPring-8 Angstrom Compact Free Electron Laser (SACLA) [19] (Fig. 1a). A high-intensity optical laser ($\sim 10^{12}$ W/cm²) launched uniaxial shock waves into the NPD samples. The compressed states were probed ~ 1 ns after shock entry using an ultrafast (< 10 fs), $\sim 10^{11}$ photons/pulse XFEL pulse [20], and diffraction patterns were captured on flat-panel pixel array detectors. The NPD samples were synthesized at Ehime University using the BOTCHAN multi-anvil press and had an initial density of 3.514(3) g/cm³ [1,2]. NPD's nano-grained microstructure (30-50 nm grains) allowed for clear and uniform diffraction measurements. In parallel, we conducted large-scale MD simulations of NPD shock-compressed to various peak stresses akin to the experiments to further reveal the underlying deformation mechanisms (Fig. 1b).

Ultra-high flow strength

We used *in situ* XRD to directly measure the lattice strains in shocked NPD and extract the material's flow strength. In NPD, the longitudinal sound speed (~ 18 km/s) is much faster than the bulk sound speed (~ 11 km/s) [21], so the material supports a two-wave shock structure—elastic followed by plastic wave—even up to multi-megabar stresses (Fig. 1c). A representative diffraction pattern is shown in Fig. 1d. In such patterns, the position of each diffraction ring encodes the spacing between atomic planes in the crystal (d-spacing), while intensity variations around the rings reflect how grains are oriented. By comparing the signal between different azimuthal sectors, we can resolve directional differences in the lattice spacing. Line profiles taken at specific azimuthal sectors are shown in Fig. 1e. The diffraction data show three distinct peaks for each reflection, corresponding to uncompressed, elastically compressed, and plastically compressed regions within the sample. The d-spacings we measure from elastically and plastically

compressed NPD vary systematically with the azimuthal angle ϕ . In some shots, the diffraction intensity also varies with ϕ , indicating development of preferred orientation, described in the next section.

Our diffraction measurements allowed us to determine the flow strength 2τ for each shot. The azimuthal variations of the d-spacing were analyzed to extract the lattice strain components along the shock direction ($\varepsilon^{\ell}_{\parallel}$) and the directions transverse to it ($\varepsilon^{\ell}_{\perp}$). The difference between these components gives the differential lattice strain, which we multiplied by the shear modulus to compute the flow strength 2τ . We also calculated flow strength from our MD simulations (Fig. 1b), where the longitudinal and transverse stresses are measured directly.

The flow strengths measured from both experiments and simulations are plotted as a function of shock stress and total strain in Fig. 2, and show an increase followed by a reduction with shock intensity. The experimentally measured strength reaches a peak value of 107 ± 5 GPa at a shock stress of 227 ± 8 GPa and total uniaxial strain of 0.262 ± 0.05 . This represents a five-fold increase compared to the ultimate strength of NPD under quasi-static compression [6]. It is also higher than other results reported on single-crystalline and micro-polycrystalline diamond under shock compression [7,10]. Furthermore, it is at least ten times higher than shock results of other materials including alumina and silicon carbide [22,23]. This result shows that under multi-megabar shock conditions, NPD achieves an unprecedented flow strength beyond what has been measured thus far in any material under any condition.

At stresses below 227 ± 8 GPa, the flow strength increases with shock stress, while at higher stresses, the strength decreases and becomes negligible at shock stresses of 565 ± 14 GPa in the experiments and 623 GPa in the simulations. Overall, the values and trends in flow strength

between experiments and MD simulations are consistent. These results demonstrate two regimes, with strain hardening followed by softening with increasing shock intensity.

Ultrafast grain reorientation from dislocation plasticity

In crystal lattices, dislocations are line defects that move along specific slip systems to carry plastic deformation [14]. In diamond, the primary slip systems are along the $\{111\}$ planes, in the $\langle 110 \rangle$ directions. Our XRD experiments provide mechanistic evidence of dislocation-mediated slip through changes in grain orientations, termed crystal texture.

Under compressive loading, plastic deformation mediated by dislocation slip typically leads to the reorientation of crystallites. This occurs because slip within grains alters their shape in specific ways, causing the grains to rotate to meet the lateral confinement requirement imposed by the plane strain shock condition. In single crystals and textured polycrystals, crystal rotation appears as movement of diffraction spots along the azimuthal angle [24]. This has been used to infer active slip systems and twinning in shocked tantalum, iron, copper and magnesium [16,25–27]. However, this approach cannot be used in an initially untextured material like NPD. Instead, we can assess grain reorientation through the emergence of crystallographic texture.

Our diffraction measurements show development of a preferred orientation in NPD shocked to 425 ± 14 GPa and above, as evidenced by azimuthal variations in diffraction intensity in the plastically compressed fraction (Fig. 3a). This reorientation of grains is detectable less than one nanosecond after the shock-wave enters the sample. Simulated diffraction patterns generated by forward modeling various textures indicate that our results are consistent with the emergence of a weak $\langle 110 \rangle$ fiber texture (Fig. 3b). This means the grains reorient such that their $\langle 110 \rangle$

directions align with the shock compression axis, while orientations transverse to this axis remain randomly distributed.

By generating simulated two-dimensional XRD patterns from the MD atomic positions at 623 GPa, we confirm consistency with the experimentally observed diffraction patterns at high stresses (Fig. 3c). Inverse pole figures from the MD results before and after compression confirm that NPD with an initially random texture forms a $\langle 110 \rangle$ fiber texture upon shock (Fig. 3e).

These results can be interpreted in the context of face-centered cubic (FCC) metals, which share much of their symmetry elements with diamond. When compressed, untextured FCC metals typically develop a $\langle 110 \rangle$ fiber texture due to slip along the $\{111\}\langle 110 \rangle$ systems within the grain interiors. This texture formation has been demonstrated both theoretically and experimentally in multiple FCC metals under a variety of loading conditions [28–33]. Therefore, we interpret the grain reorientation to a $\langle 110 \rangle$ fiber texture as evidence of increasing dislocation mediated slip within grain interiors at high stresses. We propose that this texture formation, which coincides with a reduction in flow strength, is due to a shift in the dominant plasticity mechanism, described in the next section.

Competing dislocation plasticity mechanisms

In materials with a face-centered lattice like diamond, the full dislocations ($a/2\langle 110 \rangle\{111\}$) that carry slip along the $\{111\}$ planes can dissociate into two partial dislocations ($a/6\langle 112 \rangle\{111\}$), lowering the energy barrier to plasticity. The two partials are separated by a planar defect called a stacking fault.

Our MD simulations reveal that the transition from hardening to softening at 260 GPa coincides with a shift in the predominant dislocation character (Fig. 4a). Across all stresses, both

partial and full dislocations are observed (Fig. 4b). However, the trends in dislocation densities between these two dislocation types are different.

Specifically, up to 260 GPa, increasing shock stress causes a rise in both partial and full dislocation densities. Notably, the partial dislocation densities at these stresses are higher than full dislocation densities. A grain-scale visualization illustrates that partial dislocations and stacking faults are dominant at 196 GPa (Fig. 4c). We propose that the hardening behavior in this regime is linked to the increase in partial dislocation density. The stacking faults that are bound by partial dislocations constrain dislocation motion to a specific plane, thereby reducing the mean free path of dislocations moving on other planes [34]. Therefore, we interpret that the unprecedented flow strength of 107 ± 5 GPa in shocked NPD is caused by stacking fault-mediated strain hardening. This demonstrates a new strengthening effect in diamond, in addition to the established grain boundary and nano-twin strengthening [1–3].

At higher shock stresses of 260 GPa and above, the density of full dislocations continues to increase, while the density of partials decreases. As a result, full dislocation density becomes much higher than that of partial dislocations. Visualization of the same grain at 623 GPa confirms this shift in dislocation character (Fig. 4d). We propose that the increase in full dislocation activity facilitates easier plastic flow and directly leads to both the observed softening and texture formation at these stresses.

Discussion

In this work, we report an unprecedented peak flow strength in shocked NPD, reaching five times the ultimate strength observed in NPD under quasi-static compression. Our measured peak flow strength is also higher than that measured in shocked micro-polycrystalline and single-crystalline

diamond [7,10] and is more than ten times that of other strong materials under shock, such as alumina and silicon carbide [22,23] (Fig. 2). Our results reveal clear trends in the flow strength with respect to stress and strain which have not been established previously in shocked diamond materials.

Prior studies have achieved ultrahigh hardness in diamond materials through grain boundary and nano-twin boundary strengthening. The high elastic limit reported by Katagiri *et al.* [18] in shocked NPD was also primarily attributed to grain boundary strengthening. Our findings demonstrate a new stacking fault mediated strengthening mechanism in plastically deformed diamond. Stacking faults are planar defects that, together with grain boundaries, reduce the mean free path of dislocations, thereby increasing the flow strength [34].

Notably, stacking-fault mediated strengthening was not observed in quasi-static compression experiments on NPD by Wang *et al.* [6]. Although they measured a high flow strength of 22 GPa, their post-mortem microscopy revealed very few free dislocations in the recovered NPD samples. Instead, they found nano-twins, suggesting that at lower stresses, NPD deforms primarily via nano-twinning and grain boundary sliding, with minimal dislocation activity within the grains. By contrast, our shock compression experiments achieve much higher stresses that trigger dislocation activity in NPD.

The strengthening mechanisms we observe provide context for a new emerging understanding of pressure-dependent grain boundary strengthening in nano-grained materials. Previous experiments on nano-crystalline metals have determined that as grain size is decreased, the deformation mechanism changes from dislocation-slip to grain boundary sliding [35]. This leads to a decline in strength known as inverse Hall-Petch behavior. However, theoretical and experimental studies show that the inverse Hall-Petch transition can be inhibited through the

application of pressure, which prevents grain boundary sliding [32,34,36]. In nano-crystalline nickel, compressing to high pressure enables full dislocation slip to dominate the plasticity even down to 3 nm in grain size, leading to a maximum flow strength of 10.2 GPa via traditional grain boundary strengthening [32]. Our shock experiments create ultra-high hydrodynamic pressures that similarly cause a strong confinement effect that inhibits grain boundary activity in NPD, contributing to the unusually high flow strengths. Existing MD studies of shocked nanocrystalline metals confirm that high shock stresses can influence the Hall-Petch to inverse Hall-Petch transition [34,36]. A comparison of our measured flow strengths in NPD to those of shocked micro-polycrystalline diamond [10] indicates possible Hall-Petch strengthening, consistent with the dislocation-mediated plasticity measured by our experiments and simulations.

Our findings extend to a broader class of ultrahard ceramic materials. While these materials are known to exhibit plasticity at quasi-static conditions of high pressure and temperature, few studies have been able to probe their plasticity mechanisms under extreme strain rates [11,37]. The measurement of grain reorientation to a $<110>$ fiber texture provides evidence that diamond, the hardest among ceramics, can exhibit significant dislocation-based plasticity under shock compression. Moreover, our simulations demonstrate that the specific plasticity mechanism evolves depending on the peak shock stress. These results pave the way for designing new ultrahard materials tailored to withstand specific deformation conditions for targeted applications.

References

1. Iriune, T., Kurio, A., Sakamoto, S., Inoue, T. & Sumiya, H. Ultrahard polycrystalline diamond from graphite. *Nature* **421**, 599–600 (2003).

2. Sumiya, H. & Irfune, T. Hardness and deformation microstructures of nano-polycrystalline diamonds synthesized from various carbons under high pressure and high temperature. *J. Mater. Res.* **22**, 2345–2351 (2007).
3. Huang, Q. *et al.* Nanotwinned diamond with unprecedented hardness and stability. *Nature* **510**, 250–253 (2014).
4. Kanel, G. I., Fortov, V. E. & Razorenov, S. V. Behavior of Brittle Materials under Shock-Wave Loading. in *Shock-Wave Phenomena and the Properties of Condensed Matter* (eds. Kanel, G. I., Fortov, V. E. & Razorenov, S. V.) 111–178 (Springer, New York, NY, 2004). doi:10.1007/978-1-4757-4282-4_4.
5. Weidner, D. J., Wang, Y. & Vaughan, M. T. Strength of Diamond. *Science* **266**, 419–422 (1994).
6. Wang, Y. *et al.* Plastic Deformation and Strengthening Mechanisms of Nanopolycrystalline Diamond. *ACS Nano* **15**, 8283–8294 (2021).
7. McWilliams, R.S. *et al.* Strength effects in diamond under shock compression from 0.1 to 1 TPa. *Phys. Rev. B* **81**, 014111(2010).
8. Lang, J. M., Winey, J. M. & Gupta, Y. M. Strength and deformation of shocked diamond single crystals: Orientation dependence. *Phys. Rev. B* **97**, 104106 (2018).
9. Winey, J. M., Knudson, M. D. & Gupta, Y. M. Shock compression response of diamond single crystals at multimegabar stresses. *Phys. Rev. B* **101**, 184105 (2020).
10. MacDonald, M. J. *et al.* Using simultaneous x-ray diffraction and velocity interferometry to determine material strength in shock-compressed diamond. *Appl. Phys. Lett.* **116**, 234104 (2020).

11. Katagiri, K. *et al.* Transonic dislocation propagation in diamond. *Science* **382**, 69–72 (2023).
12. Field, J. E. The mechanical and strength properties of diamond. *Rep. Prog. Phys.* **75**, 126505 (2012).
13. Brookes, C. A. & Brookes, E. J. Diamond in perspective: a review of mechanical properties of natural diamond. *Diam. Relat. Mater.* **1**, 13–17 (1991).
14. Meyers, M. A. & Chawla, K. K. *Mechanical Behavior of Materials*. (Cambridge University Press, 2008).
15. Smith, R. F. *et al.* High strain-rate plastic flow in Al and Fe. *J. Appl. Phys.* **110**, 123515 (2011).
16. Wehrenberg, C. E. *et al.* In situ X-ray diffraction measurement of shock-wave-driven twinning and lattice dynamics. *Nature* **550**, 496–499 (2017).
17. Lang, J. M., Jr. & Gupta, Y. M. Strength and elastic deformation of natural and synthetic diamond crystals shock compressed along [100]. *J. Appl. Phys.* **107**, 113538 (2010).
18. Katagiri, K. *et al.* Shock Response of Full Density Nanopolycrystalline Diamond. *Phys. Rev. Lett.* **125**, 185701 (2020).
19. Inubushi, Y. *et al.* Development of an Experimental Platform for Combinative Use of an XFEL and a High-Power Nanosecond Laser. *Appl. Sci.* **10**, 2224 (2020).
20. Ishikawa, T. *et al.* A compact X-ray free-electron laser emitting in the sub-ångström region. *Nat. Photonics* **6**, 540–544 (2012).
21. Chang, Y.-Y., Jacobsen, S. D., Kimura, M., Irifune, T. & Ohno, I. Elastic properties of transparent nano-polycrystalline diamond measured by GHz-ultrasonic interferometry and resonant sphere methods. *Phys. Earth Planet. Inter.* **228**, 47–55 (2014).

22. Ahrens, T. J., Gust, W. H. & Royce, E. B. Material Strength Effect in the Shock Compression of Alumina. *J. Appl. Phys.* **39**, 4610–4616 (1968).

23. Vogler, T. J., Reinhart, W. D., Chhabildas, L. C. & Dandekar, D. P. Hugoniot and strength behavior of silicon carbide. *J. Appl. Phys.* **99**, 023512 (2006).

24. Heighway, P. G. & Wark, J. S. Kinematics of slip-induced rotation for uniaxial shock or ramp compression. *J. Appl. Phys.* **129**, 085109 (2021).

25. Merkel, S. *et al.* Femtosecond Visualization of hcp-Iron Strength and Plasticity under Shock Compression. *Phys. Rev. Lett.* **127**, 205501 (2021).

26. Suguit, M. J. *et al.* Nanosecond white-light Laue diffraction measurements of dislocation microstructure in shock-compressed single-crystal copper. *Nat. Commun.* **3**, 1224 (2012).

27. Williams, C. L. *et al.* Real-time observation of twinning-detwinning in shock-compressed magnesium via time-resolved *in situ* synchrotron XRD experiments. *Phys. Rev. Mater.* **4**, 083603 (2020).

28. Kocks, U. F., Tomé, C. N. & Wenk, H.-R. *Texture and Anisotropy: Preferred Orientations in Polycrystals and Their Effect on Materials Properties*. (Cambridge University Press, 2000).

29. Hu, S. C. *et al.* Texture evolution in nanocrystalline Cu under shock compression. *Journal of Applied Physics* **127**, 215106 (2020).

30. Margulies, L., Winther, G. & Poulsen, H. F. In Situ Measurement of Grain Rotation During Deformation of Polycrystals. *Science* **291**, 2392–2394 (2001).

31. Hu, H. Texture of Metals. *Texture Stress Microstruct.* **1**, 753983 (1974).

32. Zhou, X. *et al.* High-pressure strengthening in ultrafine-grained metals. *Nature* **579**, 67–72 (2020).

33. Bisht, A., Kumar, L., Subburaj, J., Jagadeesh, G. & Suwas, S. Effect of stacking fault energy on the evolution of microstructure and texture during blast assisted deformation of FCC materials. *J. Mater. Process. Technol.* **271**, 568–583 (2019).

34. Li, W. *et al.* Unraveling the Hall-Petch to inverse Hall-Petch transition in nanocrystalline high entropy alloys under shock loading. *Int. J. Plast.* **178**, 104010 (2024).

35. Han, X., Wang, L., Yue, Y. & Zhang, Z. In situ atomic scale mechanical microscopy discovering the atomistic mechanisms of plasticity in nano-single crystals and grain rotation in polycrystalline metals. *Ultramicroscopy* **151**, 94–100 (2015).

36. Bringa, E. M. *et al.* Ultrahigh Strength in Nanocrystalline Materials Under Shock Loading. *Science* **309**, 1838–1841 (2005).

37. Chen, M. W., McCauley, J. W., Dandekar, D. P. & Bourne, N. K. Dynamic plasticity and failure of high-purity alumina under shock loading. *Nat. Mater.* **5**, 614–618 (2006).

Acknowledgments

We thank Paul E. Specht of Sandia National Laboratories, Patrick G. Heighway of the University of Oxford, Darshan Chalise of Stanford University, and Dayeeta Pal of Stanford University for scientific discussions. The experiments were performed at BL3 of SACLAC with the approval of the Japan Synchrotron Radiation Research Institute (proposal nos. 2019A8041, 2018B8069,). The NPD sample fabrication was conducted under the support of Joint Research Center PRIUS (Ehime University, Japan). This work was supported by grants from MEXT Quantum Leap Flagship Program (MEXT Q-LEAP) Grant No. JPMXS0118067246, Japan Society for the Promotion of Science (JSPS) KAKENHI (Grants Nos. 21J10604, 19K21866, & 16H02246), Genesis Research Institute, Inc. (Konpon-ken, Toyota), Yamada Science Foundation, and the U.S. Department of

Energy by Lawrence Livermore National Laboratory under Contract DE-AC52-07NA27344. The discussion and the manuscript preparation were partially supported by HPSTAR. The high-power drive laser installed in SACLAC EH5 was developed with the corporation of Hamamatsu Photonics. The installation of a Diffractive Optical Elements (DOE) to improve the smoothness of the drive laser pattern was supported by the SACLAC Basic Development Program. "The MD simulations were performed at A*STAR Computational Resource Centre (A*CRC)."

Author contributions

K.K and N.O. conceived the project. T.I., T.S. and N.N. prepared the NPD samples. K.K. and A.H. designed and manufactured the targets. K.K., A.H., T.R., N.O., L.E.D.M., A.A., Y.I., S.J.I., M.K., L.M., T.M., K.M., H.N., N.N., T.O., M.O., T.S., Y.S., K.S., Y.T., S.T., T.T., Y.U., M.Y. and T.Y. conducted the experiments. A.H., D.L. and R.L. analyzed the experimental data using software developed by A.H., R.H. and D.L. W.L. designed, conducted and analyzed the MD simulations. D.L. and A.H. designed, conducted and analyzed the diffraction simulations. A.H., W.L., D.L., S.E.P., K.K. and L.E.D.M. wrote the manuscript. A.H., W.L., R.L., D.L. and E.W.C. made the figures. All authors discussed the results and commented on the manuscript.

Data availability

The raw data from our X-ray diffraction experiments can be made available on reasonable request.

Competing interests

The authors declare no competing interests.

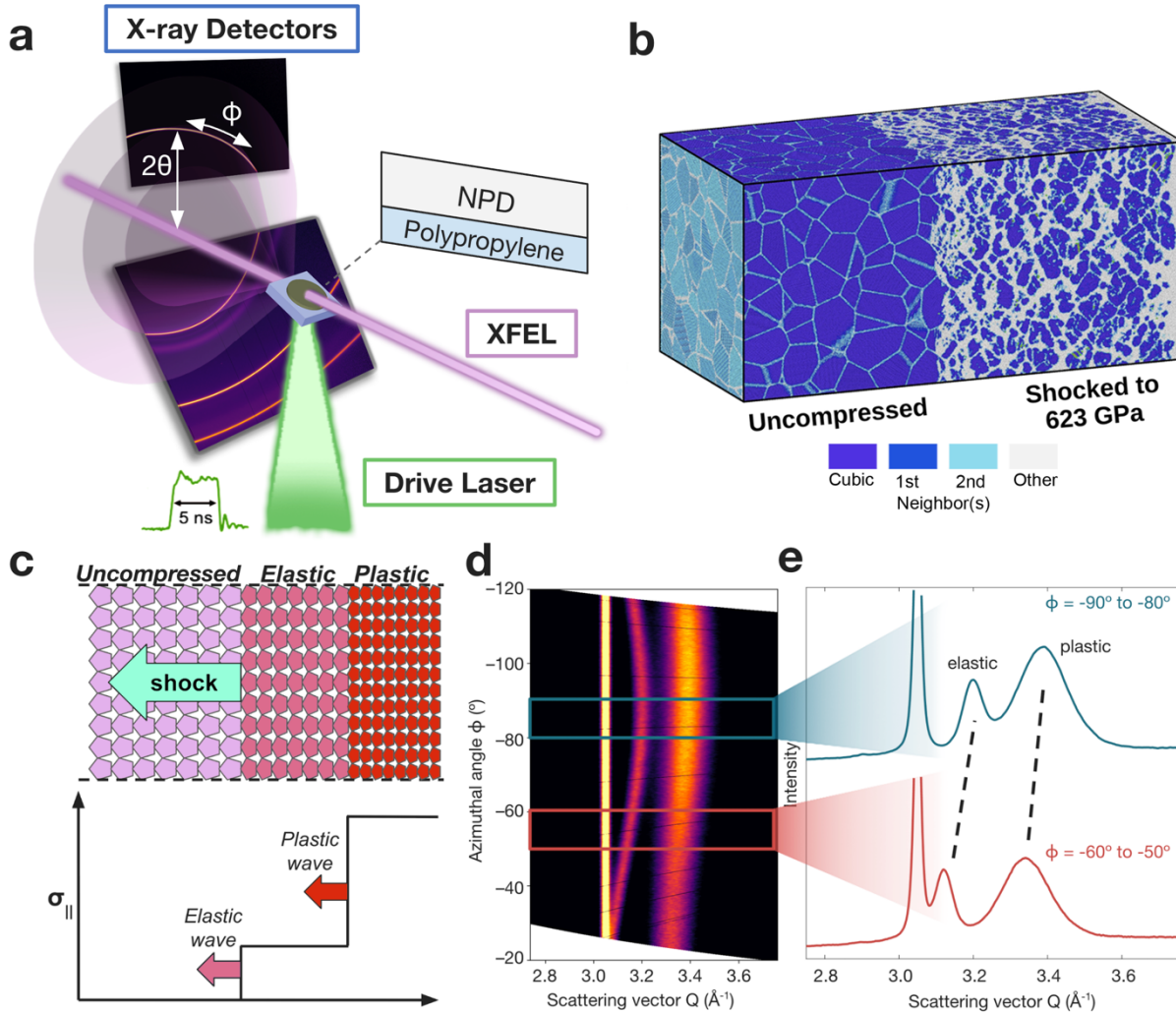


Figure 1. Shock experiments with femtosecond X-ray diffraction, and molecular dynamics simulations. **a**, Laser driven shock experiments coupled with *in situ* X-ray diffraction (XRD) using a femtosecond XFEL pulse irradiating the sample at an angle relative to the shock propagation direction. **b**, Large-scale molecular dynamics simulation consisting of 900 diamond grains shocked to 623 GPa. **c**, Schematic showing two-wave structure in uniaxially shocked NPD. The elastic wave travels faster and compresses the lattice uniaxially, while the plastic wave follows by redistributing material, allowing three-dimensional compression of the lattice. The dashed lines show the lateral confinement during shock loading. **d**, Representative XRD pattern of shocked NPD. **e**, 1D profiles are shown from specific azimuthal slices.

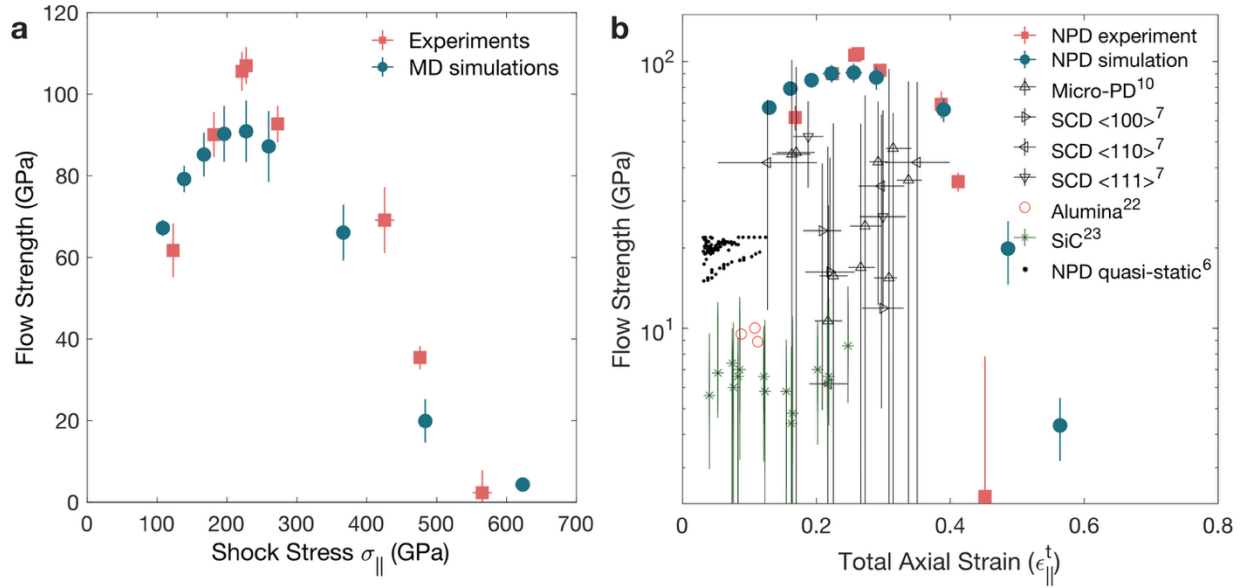


Figure 2. Ultra-high flow strength of shocked NPD. **a**, Flow strength as a function of peak shock stress. Both experiments and simulations show strain hardening up to 227 ± 8 GPa and softening at higher stresses. **b**, Logarithmic plot comparing shocked NPD's flow strength to that of other shocked materials as well as quasi-statically compressed NPD. Our measured flow strength is higher than previous measurements under shock loading, and represents a five-fold increase compared to that of quasi-statically compressed NPD.

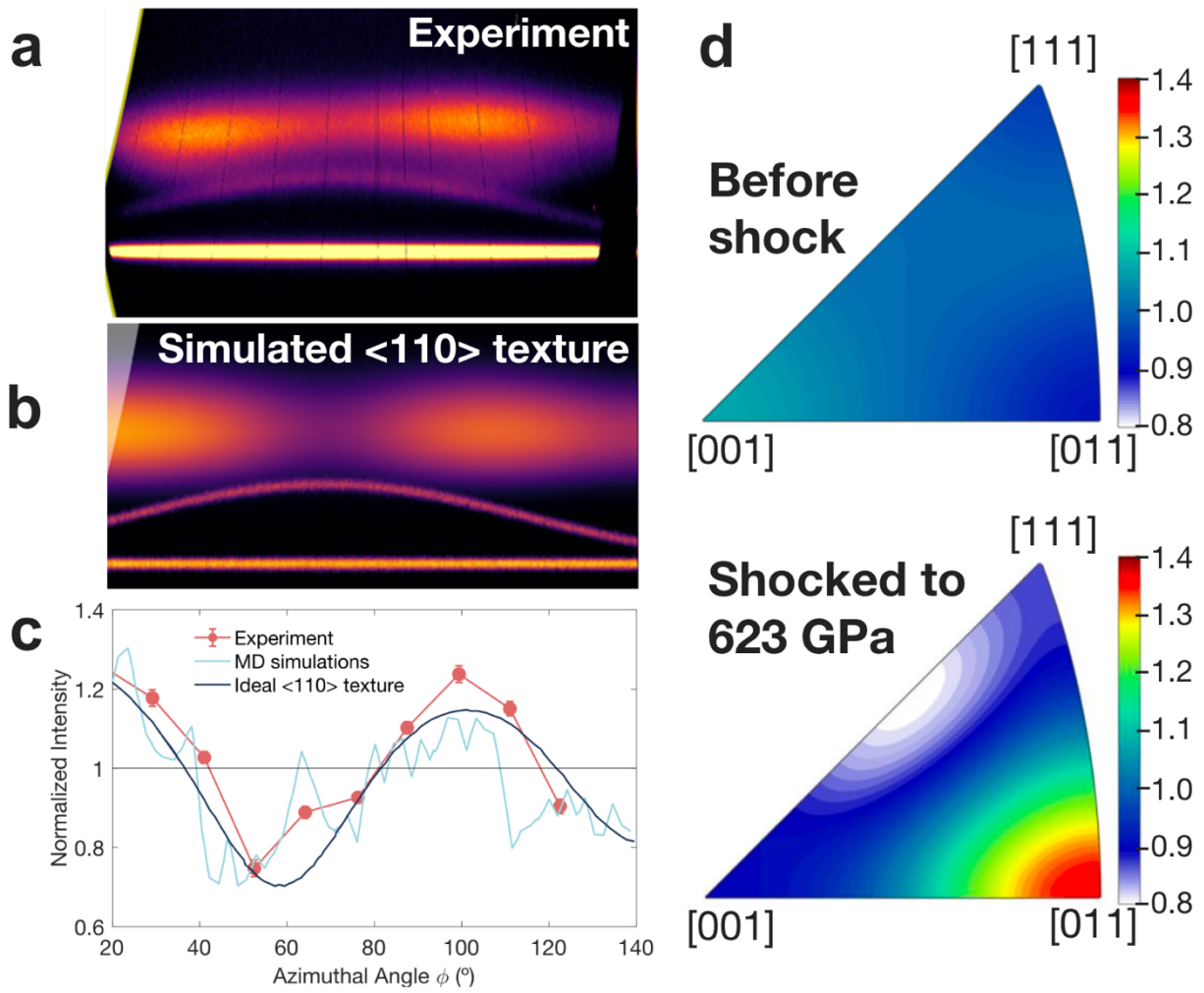


Figure 3. Ultrafast texture formation. **a**, In the high stress softening regime, diffraction from the shocked material displays azimuthal variation in intensity that is not observed in the uncompressed material. This indicates grain reorientation, i.e., formation of crystallographic texture. **b**, Diffraction pattern simulated from molecular dynamics simulations at 623 GPa shows similar texture formation. **c**, Forward model of a $<110>$ fiber texture with a mosaic spread, where the $<110>$ directions align with the shock axis and directions normal to it are randomly distributed. **d**, Line plots comparing the forward model of $<110>$ texture with the experimental and MD data as integrated intensity along ϕ . The data show good agreement with the model of $<110>$ fiber

texture. **e**, Inverse pole figures generated from molecular dynamics simulations at 623 GPa also indicate the formation of $<110>$ fiber texture.

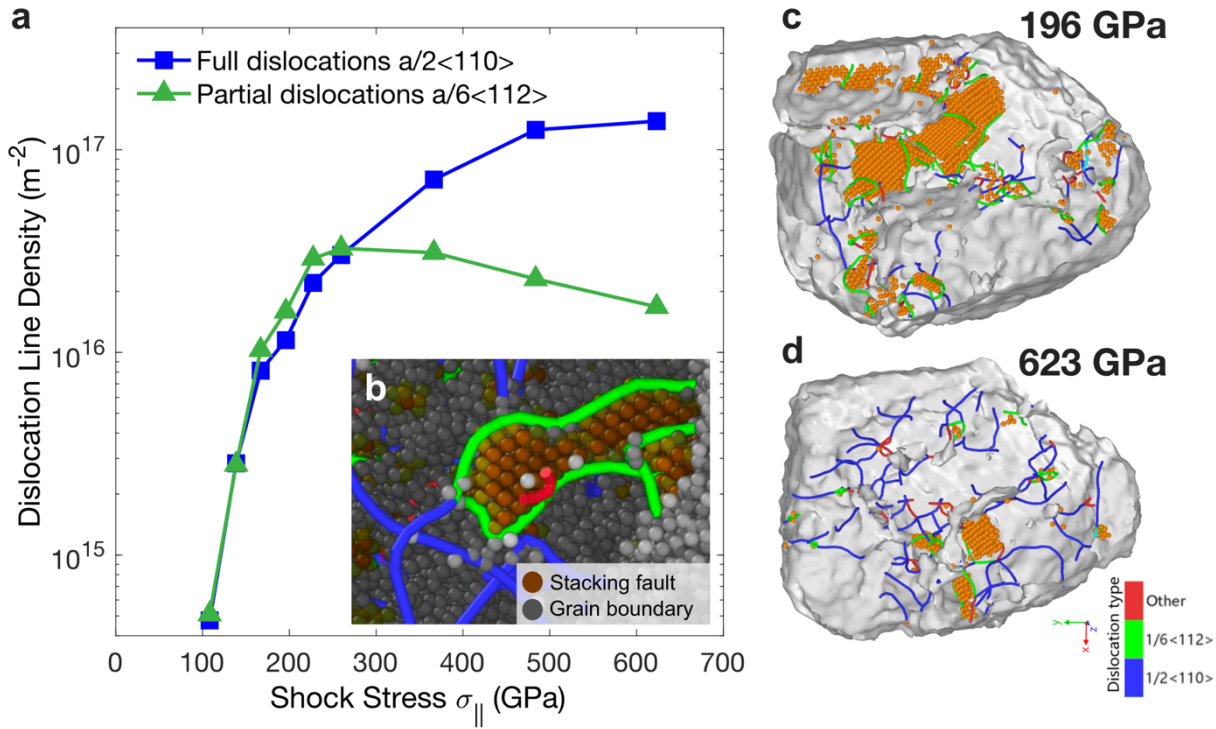


Figure 4. Evolution of dislocation character in molecular dynamics simulations. **a**, Densities of $a/6<211>$ partial and $a/2<110>$ full dislocations with increasing shock stress. Up to 260 GPa, partial and full dislocation densities increase with shock stress, with a higher density of partials. At higher stresses, the full dislocation density continues to increase, while the partial dislocation density drops off. **b**, Snapshot of a grain shocked to 196 GPa shows partial dislocations (green), stacking faults (orange atoms), and lower proportion of full dislocations (blue). **c**, Snapshot of the same grain shocked to 623 GPa shows a much higher density of full dislocations. **d**, Snapshot of a full dislocation dissociating into two partial dislocations separated by a stacking fault. For ease of visualization, cubic diamond atoms are not shown in **b**, **c** and **d**.

Methods

Sample preparation and *in situ* XRD measurements

The nano-polycrystalline diamond (NPD) samples used in this work were synthesized at the Geodynamics Research Center, Ehime University. Highly oriented pyrolytic graphite was compressed to 15 GPa and heated to 2,300-2,500 °C in the BOTCHAN 6,000-tonne multi-anvil press to form NPD.

The initial material density was $3.514 \pm 0.003 \text{ g/cm}^3$, with an average grain size of 30-50 nm [1,2]. A 15- μm thick polypropylene film glued to the NPD sample was used as an ablator to produce a single shock front while minimizing emission of hard X-rays. The laser-driven shock compression experiments were performed using a high-intensity nanosecond drive laser at the BL3 beamline at SACLAC [19]. 18 J of laser energy were focused onto a 260 μm diameter spot on the target.

The lattice and microstructure of NPD were probed using horizontally polarized, $\sim 10 \text{ fs}$ X-ray pulses produced by the SACLAC-XFEL. The X-rays were focused onto a $50 \times 20 \mu\text{m}^2$ spot on the target, which was tilted 108, 110, or 115 degrees with respect to the X-ray beam (Fig. 1, Extended Data Table 1). The X-ray energy was either 10, 11, or 12 keV, depending on the experimental run. X-ray diffraction (XRD) patterns were recorded on one or two pixel-array detectors. The delay times between the drive laser and XFEL probe pulses were tuned to probe the material within $\sim 1 \text{ ns}$ of the shock wave entering the NPD sample from the polypropylene ablator. This short time delay minimized stress gradients behind the shock-wave at the probe time. Our experiment probed the entire sample depth.

Strain under shock compression

Beyond the elastic limit of a material, the total strain ε^t consists of two components: the elastic and plastic strains,

$$\varepsilon^t = \varepsilon^e + \varepsilon^p.$$

The elastic strain, which we call the lattice strain ε^e , is the direct deformation of the crystal lattice.

The plastic strain ε^p reflects irreversible deformation of the bulk.

Under shock compression, the total strain is uniaxial due to the directionality of the shock wave and lateral confinement from the surrounding material. This constrains the strain components,

$$\varepsilon_{\parallel}^t = \varepsilon_{\parallel}^e + \varepsilon_{\parallel}^p,$$

$$\varepsilon_{\perp}^t = \varepsilon_{\perp}^e + \varepsilon_{\perp}^p = 0,$$

$$\varepsilon_{\perp}^e = -\varepsilon_{\perp}^p,$$

$$\varepsilon_{\parallel}^t = \ln(\rho/\rho_0),$$

where ε_{\perp}^t and $\varepsilon_{\parallel}^t$ are strain components along the shock direction and transverse to it, ρ_0 is the ambient density of NPD (3.514 g/cm³) and ρ is the density upon shock compression.

When the lattice deforms anisotropically, i.e., with greater compression along the shock direction than transverse to it, the projected strain on a given crystallographic plane depends on the orientation of that plane relative to the compression axis. As a result, diffraction from a given hkl reflection occurs at different d-spacings depending on the angle χ between the plane normal and the shock direction. These variations appear as warped diffraction patterns in polar plots of d-spacing versus azimuthal angle (ϕ).

Behind the shock wavefront, plastic flow causes the material to yield and displace laterally. Because lateral confinement enforces a uniaxial total strain, the outward plastic strain is counteracted by a compressive lattice strain in the transverse directions ($\varepsilon_{\perp}^e = -\varepsilon_{\perp}^p$). This leads to

a three-dimensional lattice strain. As the material loses its flow strength, it approaches the hydrodynamic limit where $\varepsilon^{\ell_{\perp}} = \varepsilon^{\ell_{\parallel}}$.

XRD Analysis

The first portion of XRD analysis was conducted following the method laid out in [38]. Positions and orientations of the X-ray detectors were determined using diffraction from a CeO₂ calibrant and cross-checked with diffraction from the uncompressed NPD starting material. This calibration was first done in Dioptas, then refined using HEXRD (39,40). HEXRD was then used to transform the images to polar coordinates and perform Lorentz-polarization and pixel solid angle corrections.

The determination of lattice strains from the measured diffraction angle required multiple steps. The variation in 2θ with respect to the azimuthal angle was determined by dividing the de-warped diffraction patterns into 10-degree azimuthal slices. Each slice was azimuthally averaged, and the resulting one-dimensional lineout from each slice was fit to a PearsonVII peak shape. The lineouts of these slices are shown for each shot in Extended Data Figures 5–13. The fit values of 2θ were then used to determine lattice strain and density of the shocked material, as described in the next section. The fits were also used to produce texture plots by observing the variation in the normalized area of the plastic peak with azimuthal angle. To ascertain the error on these fits, a final local least-squares refinement step is performed. From this least-squares step, the covariance matrix is calculated and used to extract fitting errors for each of the peak parameters. For further calculations, the errors were propagated in quadrature.

Determination of Lattice Strains and Flow Strengths

Diamond's strength leads to anisotropic lattice strain in the shocked sample, i.e., the lattice strain is greater along the longitudinal (shock) direction than along the transverse directions. We define

$\varepsilon_{zz}^l = \varepsilon_{\parallel}^l$ as the true longitudinal lattice strain component aligned with the direction of shock propagation, and $\varepsilon_{xx}^l = \varepsilon_{yy}^l = \varepsilon_{\perp}^l$ as the true transverse lattice strains perpendicular to the shock direction, which are assumed to be symmetric due to the isotropic nature of NPD.

We determined $\varepsilon_{\parallel}^l$ and ε_{\perp}^l in the shocked NPD by using the variation in measured 2θ values across different azimuthal slices. To do this, we performed an optimization in Matlab using the non-linear least squares method (lsqnonlin). The function that was optimized, Strain_Residuals.m, took in an initial guess for the lattice strain components and our experimentally measured 2θ and ϕ values. By performing the calculation laid out below, this function used the guessed lattice strain components to calculate 2θ values at each azimuthal angle. These calculated 2θ values were compared to our experimentally measured 2θ values, and the residuals between them were calculated, weighted by the uncertainties $\sigma_{2\theta}$ of the measured 2θ values,

$$\text{residual}(\phi) = \frac{2\theta_{\text{model}}(\phi) - 2\theta_{\text{measured}}(\phi)}{\sigma_{2\theta_{\text{measured}}}(\phi)}.$$

These residuals were used as input to the lsqnonlin optimization method, which repeatedly ran Strain_Residuals.m with new inputs and optimized the lattice strain components to minimize the sum of squares of the residuals. Uncertainties in the lattice strain components were quantified by using a Monte Carlo approach of randomly choosing inputted values of measured 2θ from a normal distribution with a standard deviation equivalent to the measurement uncertainty, running the optimization 2000 times, and taking the mean and standard deviation of the outputted lattice strains.

The calculation of 2θ values from guessed lattice strain components is derived as follows. Due to the uniaxial planar shock loading, we take the shock and transverse directions as principal axes and assume no shear stresses or shear strains along these axes [41,42]. This approximation is justified due to our early probe timing (~ 1 ns after shock entry into the sample) while the shock is

still planar. The deformation gradient tensor at the lattice level, \mathbf{F}^ℓ , is thus diagonal in this coordinate system, and can be written as

$$\mathbf{F}^\ell = \begin{bmatrix} \exp(\epsilon_{\perp}^\ell) & 0 & 0 \\ 0 & \exp(\epsilon_{\perp}^\ell) & 0 \\ 0 & 0 & \exp(\epsilon_{\parallel}^\ell) \end{bmatrix}.$$

Our diffraction patterns contain traces that can be described by a diffraction angle 2θ and azimuthal angle ϕ . These angles together determine the normal direction of the diffracting plane. Let \mathbf{n}_0 be the unit vector normal to the diffracting plane in the undeformed (ambient) configuration. This initial normal direction is determined for each azimuthal sector from the $2\theta_0$ of the undeformed crystal,

$$2\theta_0 = 2 \arcsin\left(\frac{\lambda}{2d_0}\right).$$

and the ϕ value of that sector, from the relation

$$\hat{\mathbf{n}}_0 = \left(\sin\left(\frac{2\theta_0}{2}\right) \cos \phi, \sin\left(\frac{2\theta_0}{2}\right) \sin \phi, \cos\left(\frac{2\theta_0}{2}\right) \right).$$

Under deformation, the unit vector that describes the plane normal direction transforms via the inverse transpose of the deformation gradient,

$$\hat{\mathbf{n}}_{\text{strained}} = \frac{\mathbf{F}^{\ell^{-T}} \hat{\mathbf{n}}_0}{|\mathbf{F}^{\ell^{-T}} \hat{\mathbf{n}}_0|}.$$

Given the diagonal form of \mathbf{F}^ℓ , this simplifies to

$$\hat{\mathbf{n}}_{\text{strained}} = \frac{\begin{bmatrix} \exp(-\epsilon_{\perp}^\ell) n_x \\ \exp(-\epsilon_{\perp}^\ell) n_y \\ \exp(-\epsilon_{\parallel}^\ell) n_z \end{bmatrix}}{\sqrt{\exp(-2\epsilon_{\perp}^\ell)(n_x^2 + n_y^2) + \exp(-2\epsilon_{\parallel}^\ell)n_z^2}}.$$

We define the angle χ as the angle between the strained plane normal and the shock direction, where

$$\cos \chi = \hat{\mathbf{n}}_{\text{strained}} \cdot \hat{\mathbf{z}}.$$

The lattice strain along the plane normal is then computed by projecting the full strain tensor onto $\hat{\mathbf{n}}_{\text{strained}}$, yielding

$$\epsilon_d^\ell = \epsilon_{\parallel}^\ell \cos^2 \chi + \epsilon_{\perp}^\ell \sin^2 \chi.$$

This leads to the change in d-spacing for the plane under the predicted strain,

$$d = d_0 \cdot \exp(-\epsilon_d^l),$$

where d_0 is the ambient d-spacing of the diffracting plane, and is given by

$$d_0 = \frac{a_0}{\sqrt{h^2+k^2+l^2}}.$$

In this equation, a_0 is the ambient lattice parameter of NPD (3.567 Å) and h, k and l are the miller indices of the diffracting plane.

Using Bragg's law, we obtain the predicted diffraction angle

$$2\theta = 2 \cdot \arcsin\left(\frac{\lambda}{2d}\right),$$

where λ is the X-ray wavelength. This method produces results that are consistent with previous work that derived a closed-form equation relating the d-spacing and lattice strain components for arbitrarily strained samples [41].

Once the lattice strain components are optimized, density (ρ) of the strained sample is calculated from the ambient density (ρ_0) and lattice strain, as follows:

$$\rho = \frac{\rho_0}{(2-\exp(\epsilon_{\parallel}^l))(2-\exp(\epsilon_{\perp}^l))^2}.$$

We determined the flow strength 2τ of the shock-compressed NPD using the relation

$$2\tau = \sigma_{\parallel} - \sigma_{\perp} = 2G(\epsilon_{\parallel}^l - \epsilon_{\perp}^l),$$

where G is the shear modulus. To estimate G , we used the Voigt iso-strain approximation from high-pressure elastic constants of diamond calculated with density functional theory (DFT) [43].

$$G = \frac{C_{11} - C_{12} + 3C_{44}}{5}.$$

Note that the flow strength is defined as twice the maximum shear stress τ [44]. This is also equivalent to the differential stress sustained by the material during deformation.

Determination of Peak Shock Stresses

The peak longitudinal stress under plastic deformation (σ_{\parallel}) was determined for each run from the measured densities using the linear U_s - u_p (shock velocity - particle velocity) relation of full-density NPD, which has been experimentally determined by Katagiri *et al.*, 2020 [7]. The samples used by Katagiri *et al.* were made by the same supplier as those used in the present work.

The U_s - u_p fit derived from the measurements was used along with the Rankine-Hugoniot conservation equations for mass ($\frac{\rho_0}{\rho} = \frac{U_s - u_p}{U_s}$) and momentum ($\sigma_{\parallel} = \rho_0 U_s u_p$) to determine longitudinal stress from density during shock propagation, $\sigma_{\parallel} = \rho u_p (U_s - u_p)$.

Forward Model Diffraction Simulations

Fiber diffraction patterns were simulated in Python using a proprietary GPU-accelerated Monte-Carlo method. Three-dimensional coordinates were defined with the convention of the z-axis pointing out of the page, x-axis pointing to the right, and y axis pointing up. All calculations were done from a reference frame in which the beam direction was defined as pointing along the -z axis. The shock direction was defined as a 108, 110 or 115 degree rotation of the beam direction about the x axis (Fig. 1, Extended Data Table 1).

First, diamond's crystallographic planes were defined as unit vectors pointing in the direction normal to the plane. These plane normal vectors were then rotated such that the crystallographic direction corresponding to the fiber axis was aligned with the shock direction. The Monte-Carlo engine assigns a random (uniformly distributed) twist between 0° and 360° and a mosaic spread away from the fiber axis (using a gaussian distribution = 10°) to each grain. For every grain, the X-ray beam was analytically reflected from each plane; if the reflection's wavelength satisfied

$$|\lambda - 2d \sin \theta_b| < \Delta\lambda,$$

where $\Delta\lambda$ corresponds to the X-ray bandwidth. Corresponding polar (2θ) and azimuthal (ϕ) angles are then recorded, provided they also lay within the detector window. In this case 5×10^9 grains were simulated. Scherrer broadening of these recorded points for 30 nm crystallites is then applied. It must be noted that we are not claiming that the NPD reached an orientation distribution where the greatest misorientation angle from the fiber axis was 10° . This degree of mosaicity was chosen for ease of comparison between the data and simulations. Since the NPD began with a fully random orientation distribution, it is to be expected that some portion of the texture remains random, even as a preferred orientation emerges.

Large-Scale Molecular Dynamics Simulations

A series of large-scale MD simulations were carried out to investigate the shock response of nanocrystalline Diamond using LAMMPS [45]. A quantum-accurate machine learning, Spectral Neighbor Analysis Potential (SNAP)-ML-IAP for diamond [46] was used in our work. This machine learning potential has been demonstrated in its capability of describing diamond's properties at extreme conditions spanning pressures from 0 to 50 Mbars and temperatures up to 20,000 K, including the phase diagram and melting curve of diamond with high accuracy. We also

calculate the Hugoniot curve of NPD, including the pressure versus particle velocity, which shows good agreement with experimental measurements from [7] (see Extended Data Figure 1).

The simulated NPD samples are generated using a Voronoi-construction method. In order to eliminate any size effect resulting from the number of grain boundaries in the cross section of the sample and to ensure sufficient number of grains for texture analysis, the length of the simulated system is $\sim 50.5 \times 50.5 \times 150.8 \text{ nm}^3$ along x-, y-, and z- dimensions, respectively, with the number of atoms up to 66 million. The initial model contains about 900 grains with an average grain size of $\sim 8 \text{ nm}$. Prior to shock loading, the simulated systems are relaxed under the isothermal-isobaric (NPT) ensemble which maintains constant temperature and constant pressure applied, and equilibrated at 300 K for 30 ps.

In shock MD simulations, we adopt a “piston” method which uses a virtual piston wall that impinges upon the sample such that the particle velocity in the sample is the same as the piston speed after the shock reaches steady state. In detail, with periodic boundaries along the x, and y dimensions and a free surface along the z direction, planar shock loading is achieved along the z direction by introducing a flat-surface, infinite-mass piston moving in the positive z direction from the lower z boundary. During the whole shock loading, the system is maintained under a microcanonical (NVE) ensemble where the particle number (N), volume (V), and energy (E) are consistent. corresponding to an isolated system that cannot exchange heat or matter with the outer environment. A timestep of 1 fs is used. This methodology creates shock with uniaxial total strain. The shock wave is held as it propagates to the rear free surface along the z direction.

The virial stress definition is used, where the stress tensor component for atom i is

$$\sigma_{\alpha\beta} = -\frac{1}{\Omega_i} [m_i v_{i,\alpha} v_{i,\beta} + \frac{1}{2} \sum_{n=1}^{N_p} (r_{1\alpha} F_{1\beta} + r_{2\alpha} F_{2\beta}) + \frac{1}{3} \sum_1^{N_a} r_{1\alpha} F_{1\beta} + r_{2\alpha} F_{2\beta} + r_{3\alpha} F_{3\beta}],$$

where Ω_i , m_i and v_i are the atomic volume, mass, and velocity of atom i , respectively. The first term is a thermal kinetic energy contribution, in which the binned center-of-mass translational velocity has been subtracted. In the second term, n loops over the N_p pairwise neighbors of atom i , and the third term is for the N_a angular (three-body) interactions that involve atom i . In these terms, r_1 , r_2 , and r_3 are the positions of atoms in the pairwise or three-body interactions, and F_1 , F_2 , and F_3 are the resulting pairwise or three-body forces on those atoms.

By averaging among a group of atoms and subtracting the local center-of-mass velocity along the shock direction, we calculate the temperature

$$T = \frac{1}{2Nk_b} \sum_{i=1}^N m_i (v_{i,x}^2 + v_{i,y}^2),$$

where k_b is Boltzmann's constant, m_i is the atomic mass of atom i , and $v_{i,x}$; $v_{i,y}$ are components of the particle velocity.

Under uniaxial strain compression, the longitudinal stress (σ_{\parallel}) along the loading axis (Z) is the shock stress, and there are also non-zero stress components along the lateral directions, denoted as the X and Y axes, respectively. The hydrodynamic pressure is calculated as

$$P = -\frac{\sigma_{11} + \sigma_{22} + \sigma_{33}}{3}$$

and the von Mises flow stress is calculated using

$$\sigma_{\text{flow}} = \sqrt{\frac{(\sigma_{11} - \sigma_{22})^2 + (\sigma_{22} - \sigma_{33})^2 + (\sigma_{33} - \sigma_{11})^2}{2}}.$$

Notably, when $\sigma_{11} = \sigma_{22}$, which holds for isotropic materials under uniaxial strain, the flow stress simplifies to

$$\sigma_{\text{flow}} = \sigma_{33} - \sigma_{11} = \sigma_{\parallel} - \sigma_{\perp}.$$

This is analogous to the expression used to determine flow stress from the experiments.

To analyze the shock response in the MD simulations, the system is divided into bins along the z-axis shock direction in which local physical quantities are averaged, including components of the stress tensor, particle velocity, temperature, density, etc. Each bin has a width of twice the lattice constant ($\sim 3.57 \text{ \AA}$ at 300 K). OVITO [47] is used in all visualizations in this work. Many techniques including Identify diamond structure, Dislocation analysis (DXA), Polyhedral template matching, Grain segmentation are utilized in microstructure analysis of NPD. Inverse pole figures and statistics of misorientation angle to $\langle 110 \rangle$ are used for texture analysis.

Diffraction Patterns Simulated from Molecular Dynamics Simulations

The atomic position file outputs from the MD simulations were used as inputs to a proprietary GPU-accelerated Python atomistic wave-optics simulation. To gain better statistics, a number of additional MD simulation outputs were combined to form a total sample with 1180 grains.

This simulation initializes an X-ray beam as a finite $\sim 10^{-3}$ bandwidth plane wave and tracks the individual scattering of the wave on each atom based on

$$E_s = E_i(f_0(|\vec{q}|) + f_1(\lambda) + if_2(\lambda)),$$

where f_0, f_1, f_2 are the atomic scattering factors of each species which alter the magnitude and phase of the wavefield. Scattered wavefields are then propagated and accumulated on the detector pixels. The imported atomic positions were aligned so that the shock axis and incoming beam direction matched the experimental conditions.

38. Hari, A. *et al.* High pressure phase transition and strength estimate in polycrystalline alumina during laser-driven shock compression. *J. Phys. Condens. Matter* **35**, 094002 (2022).

39. Prescher, C. & Prakapenka, V. B. DIOPTAS: a program for reduction of two-dimensional X-ray diffraction data and data exploration. *High Press. Res.* **35**, 223–230 (2015).

40. Boyce, D. & Bernier, J. *heXRD: Modular, Open Source Software for the Analysis of High Energy X-Ray Diffraction Data.* <https://www.osti.gov/servlets/purl/1062217/> (2013) doi:10.2172/1062217.

41. Higginbotham, A. & McGonegle, D. Prediction of Debye-Scherrer diffraction patterns in arbitrarily strained samples. *J. Appl. Phys.* **115**, 174906 (2014).

42. MacDonald, M. J. *et al.* Calculation of Debye-Scherrer diffraction patterns from highly stressed polycrystalline materials. *J. Appl. Phys.* **119**, 215902 (2016).

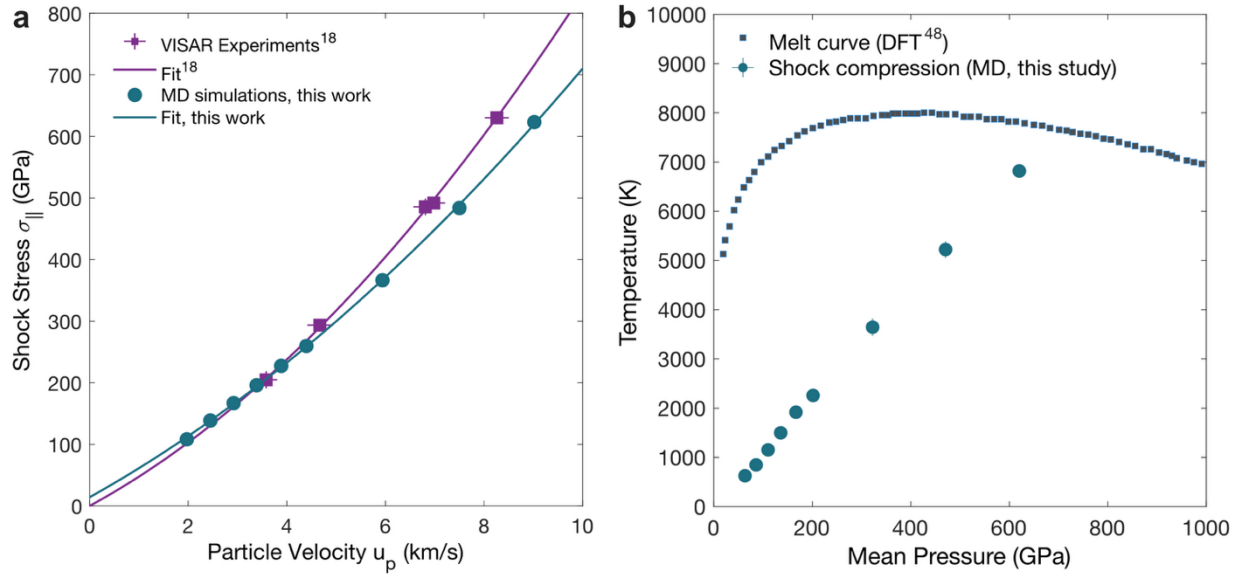
43. Zhi-Jian, F., Guang-Fu, J., Xiang-Rong, C. & Qing-Quan, G. First-Principle Calculations for Elastic and Thermodynamic Properties of Diamond. *Commun. Theor. Phys.* **51**, 1129 (2009).

44. Vogler, T. J. & Chhabildas, L. C. Strength behavior of materials at high pressures. *Int. J. Impact Eng.* **33**, 812–825 (2006).

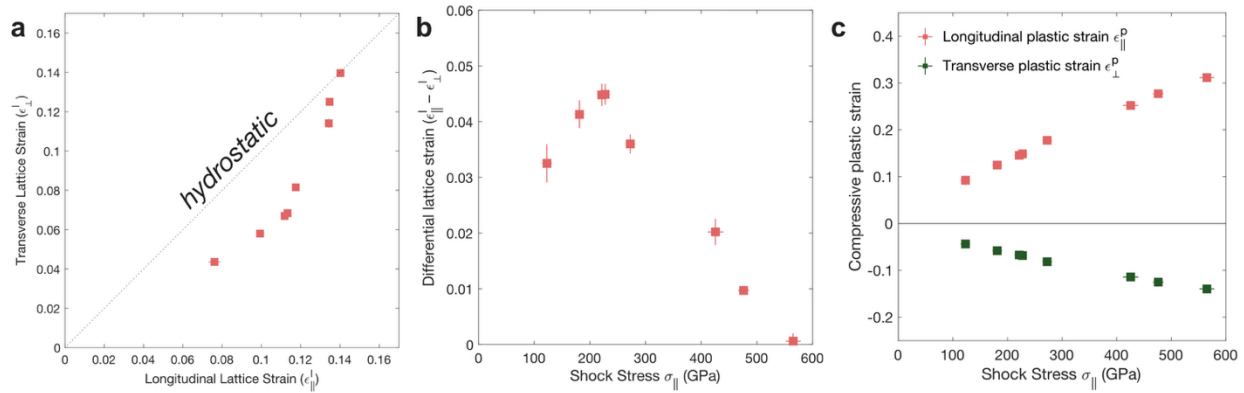
45. Thompson, A. P. *et al.* LAMMPS - a flexible simulation tool for particle-based materials modeling at the atomic, meso, and continuum scales. *Comput. Phys. Commun.* **271**, 108171 (2022).

46. Willman, J. T. *et al.* Quantum accurate SNAP carbon potential for MD shock simulations. *AIP Conf. Proc.* **2272**, 070055 (2020).

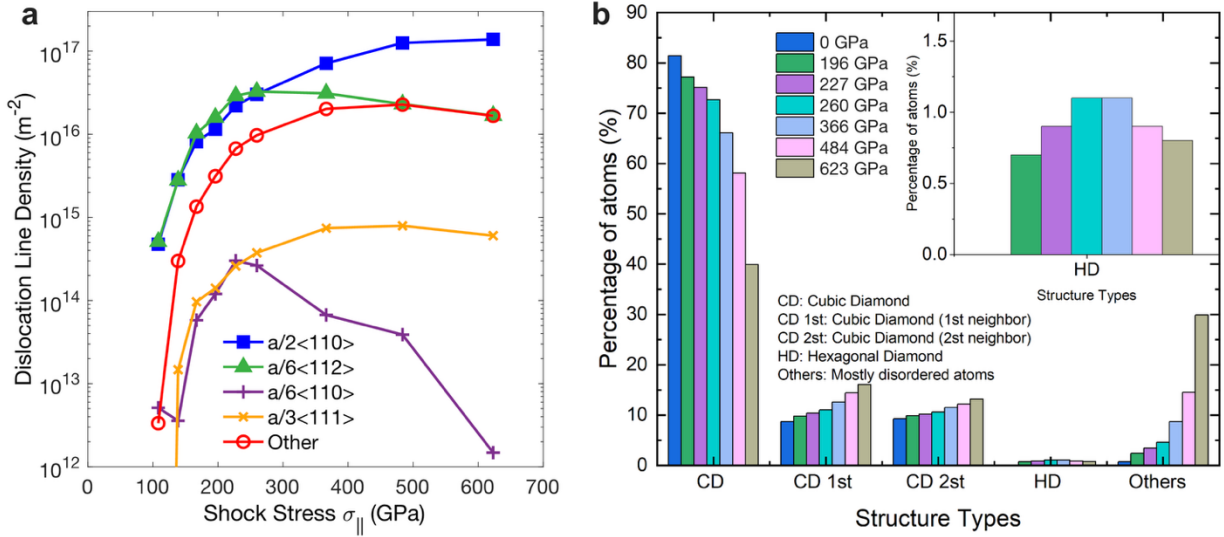
47. Stukowski, A. Visualization and analysis of atomistic simulation data with OVITO—the Open Visualization Tool. *Model. Simul. Mater. Sci. Eng.* **18**, 015012 (2009).
48. Brygoo, S. *et al.* Laser-shock compression of diamond and evidence of a negative-slope melting curve. *Nat. Mater.* **6**, 274–277 (2007).
49. Li, W. *et al.* On the grain size dependence of shock responses in nanocrystalline sic ceramics at high strain rates. *Acta Mater.* **200**, 632–651 (2020).



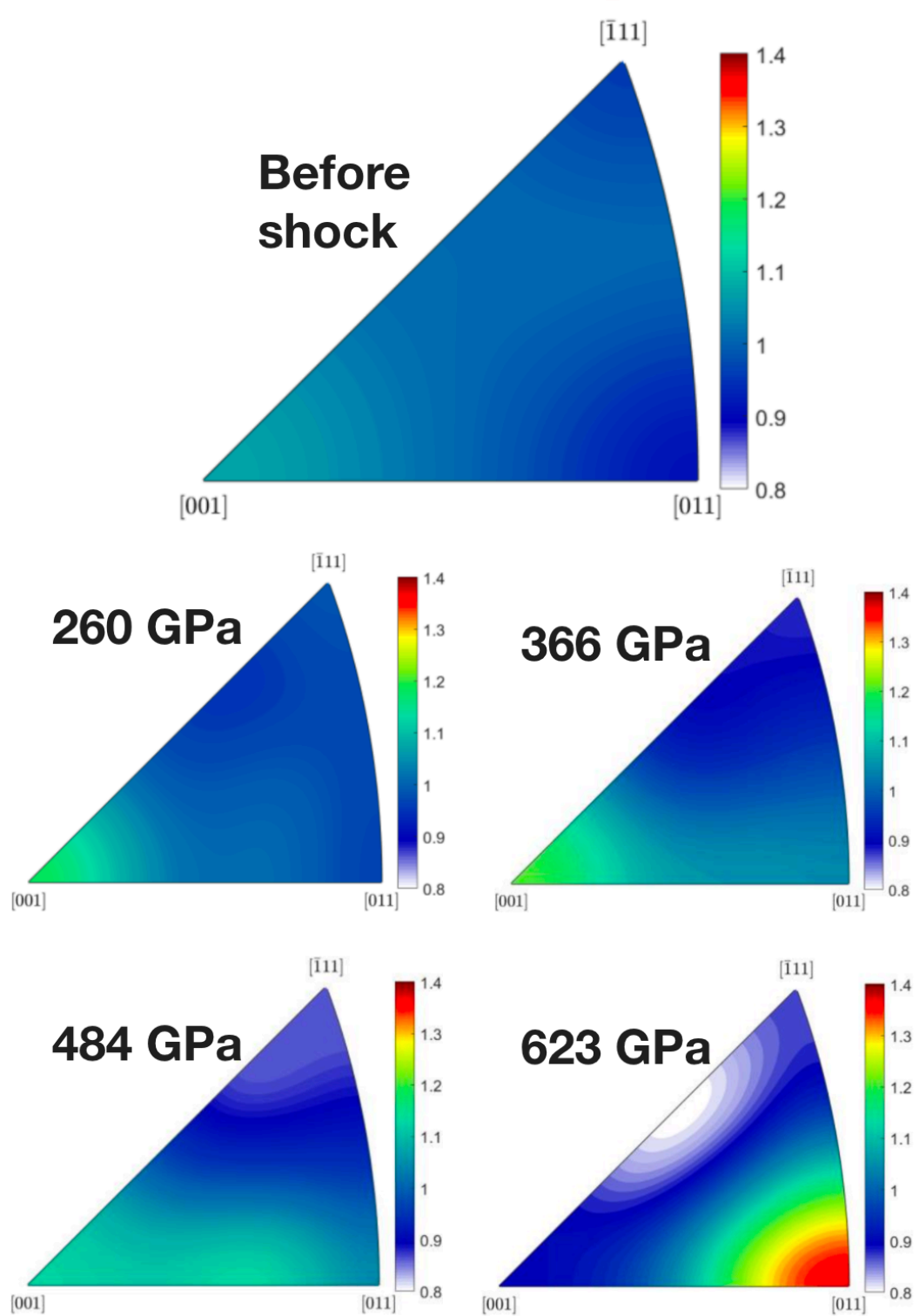
Extended Data Figure 1. Shock Hugoniot data from MD simulations. **a**, Shock Hugoniot curve of NPD from MD results of this work, compared with experimental results from Katagiri et al, 2020. Shock stress is shown as a function of particle velocity. We used the results from Katagiri et al to determine shock stress in our experimental work. **b**, Temperature vs mean pressure of shocked diamond, shown together with DFT-calculated melting curve of diamond [48]. Mean pressure is calculated as the average of stresses along the shock direction and two transverse directions, $P_M = \frac{1}{3}(\sigma_{\parallel} + 2\sigma_{\perp}) = \sigma_{\parallel} - 4/3\tau$.



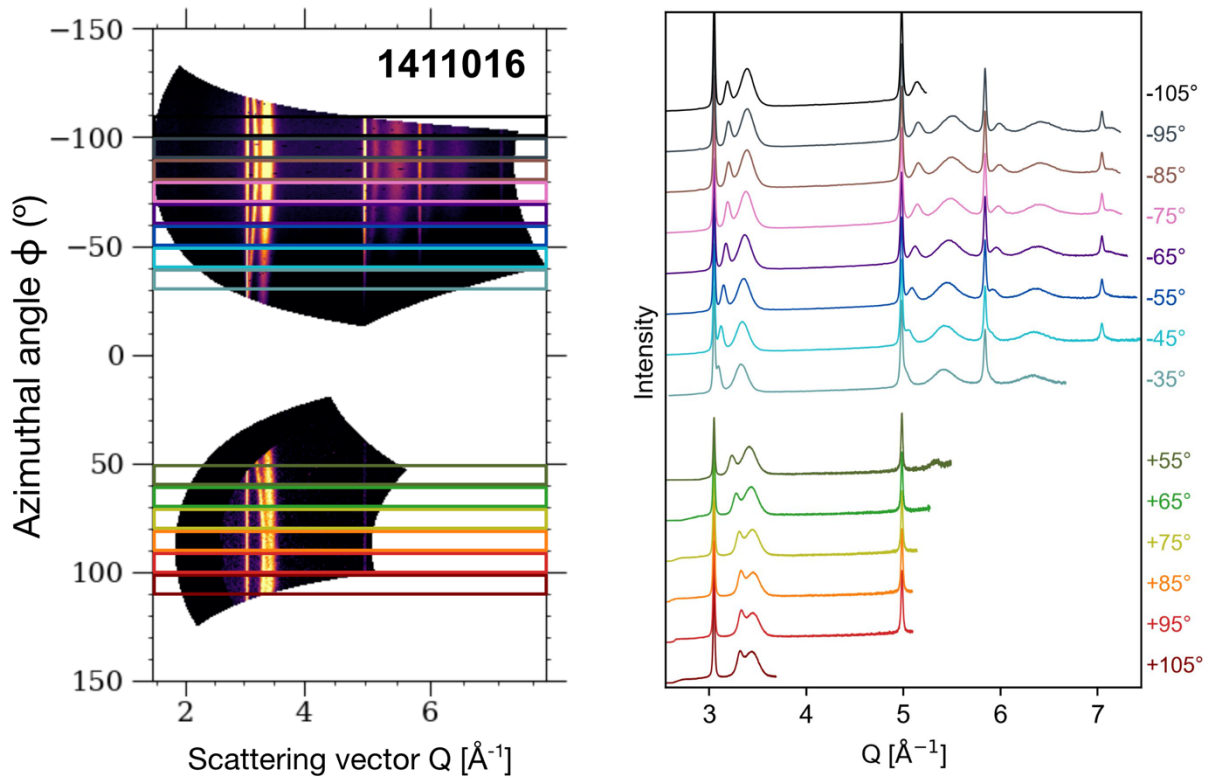
Extended Data Figure 2. Lattice strains from *in situ* XRD. **a**, Longitudinal vs transverse lattice strains are shown for our experimental results and compared to hydrostatic compression (zero strength). **b**, Differential lattice strains from our experiments are plotted as a function of peak stress. **c**, Longitudinal and transverse plastic strains, calculated from the measured lattice strains, are plotted as a function of peak stress. All strains shown are compressive strains, i.e., positive values indicate compression while negative values indicate expansion.



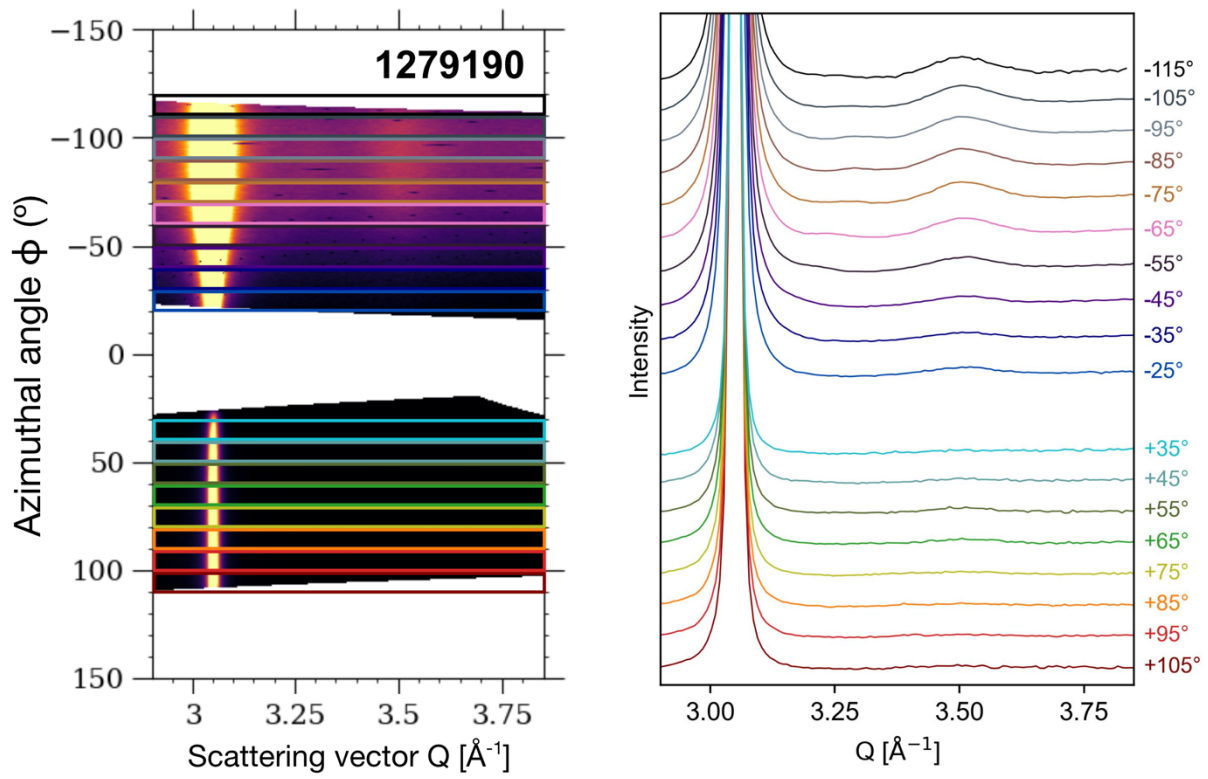
Extended Data Figure 3. Crystal structure and defects. **a**, Dislocation densities from MD simulations as a function of shock stress for various dislocation characters. The densities are normalized to the proportion of atoms in cubic diamond structure. **b**, Proportion of atoms in different structures. The hexagonal diamond structure results from stacking faults in the material.



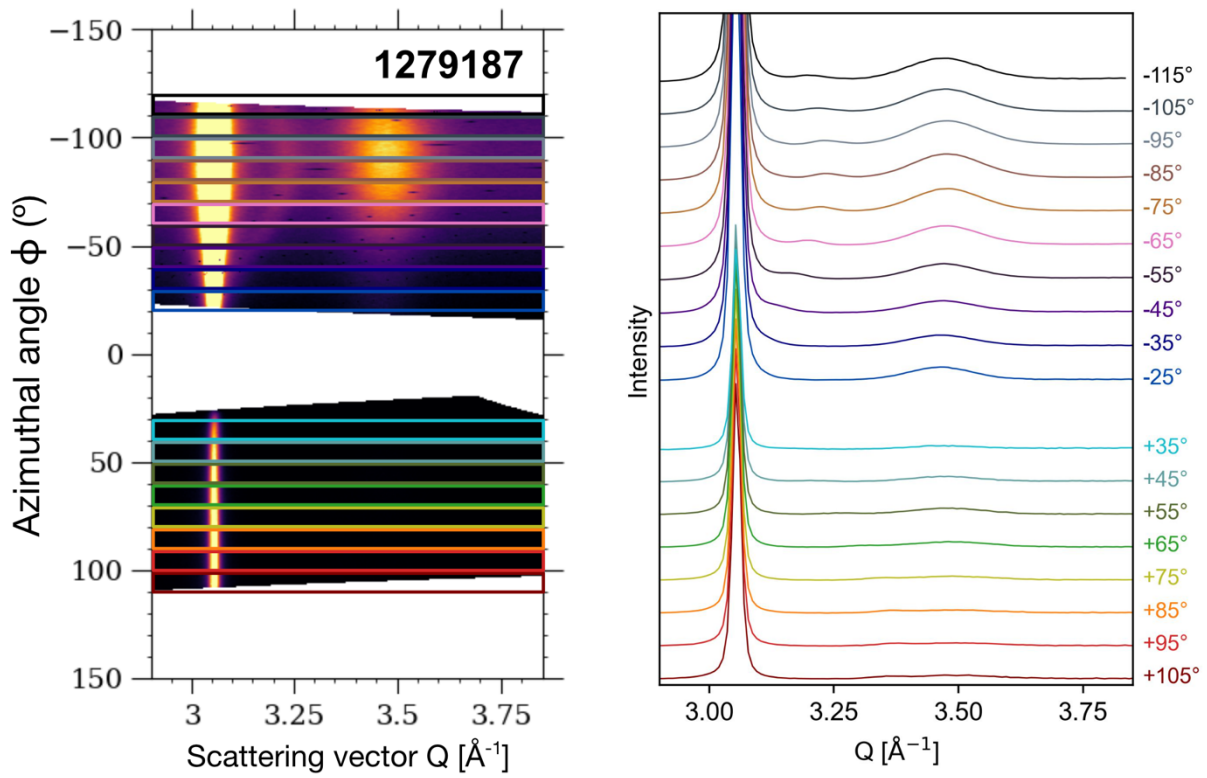
Extended Data Figure 4. Grain reorientation from MD data. Inverse pole figures from MD data at various shock stresses.



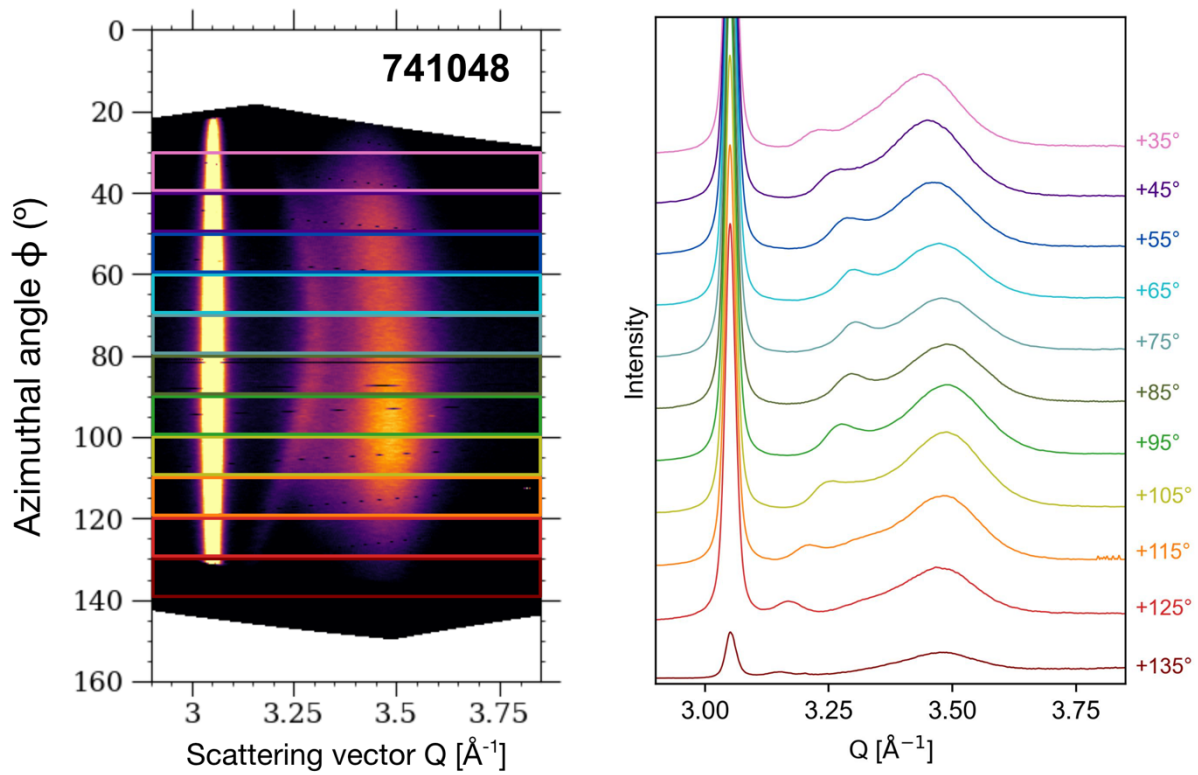
Extended Data Figure 5. Example diffraction pattern and azimuthal slices. Shown is an example diffraction pattern of NPD shocked to 227 ± 8 GPa, with flow strength of 107 ± 5 GPa. To determine the differential lattice strains used to calculate strength, the diffraction pattern was sliced into 10-degree azimuthal sectors, shown to the right. The flow strength is determined from the degree of variation of the scattering vector Q with respect to azimuthal angle.



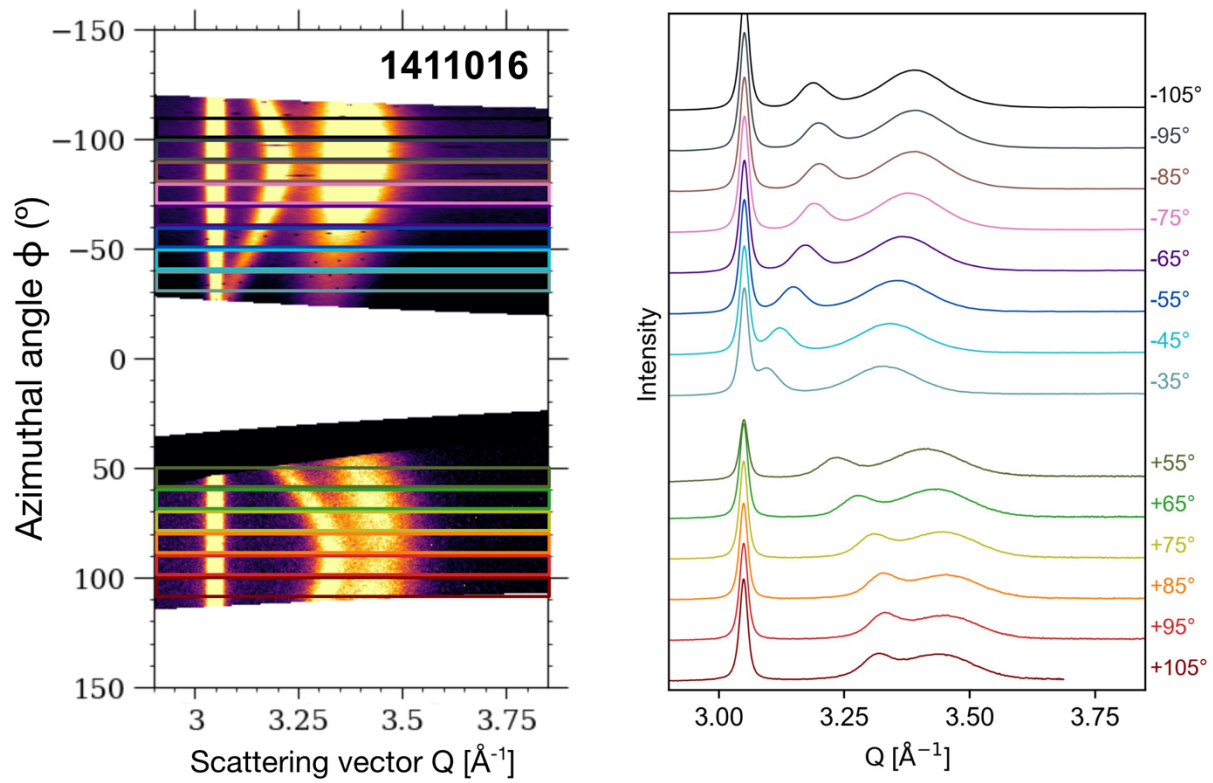
Extended Data Figure 6. Diffraction pattern of Run 1279190 (NPD shocked to 565 ± 14 GPa), with lineouts from each 10-degree azimuthal sector. To show the azimuthal variations more clearly, only diffraction from the $\{111\}$ planes is included.



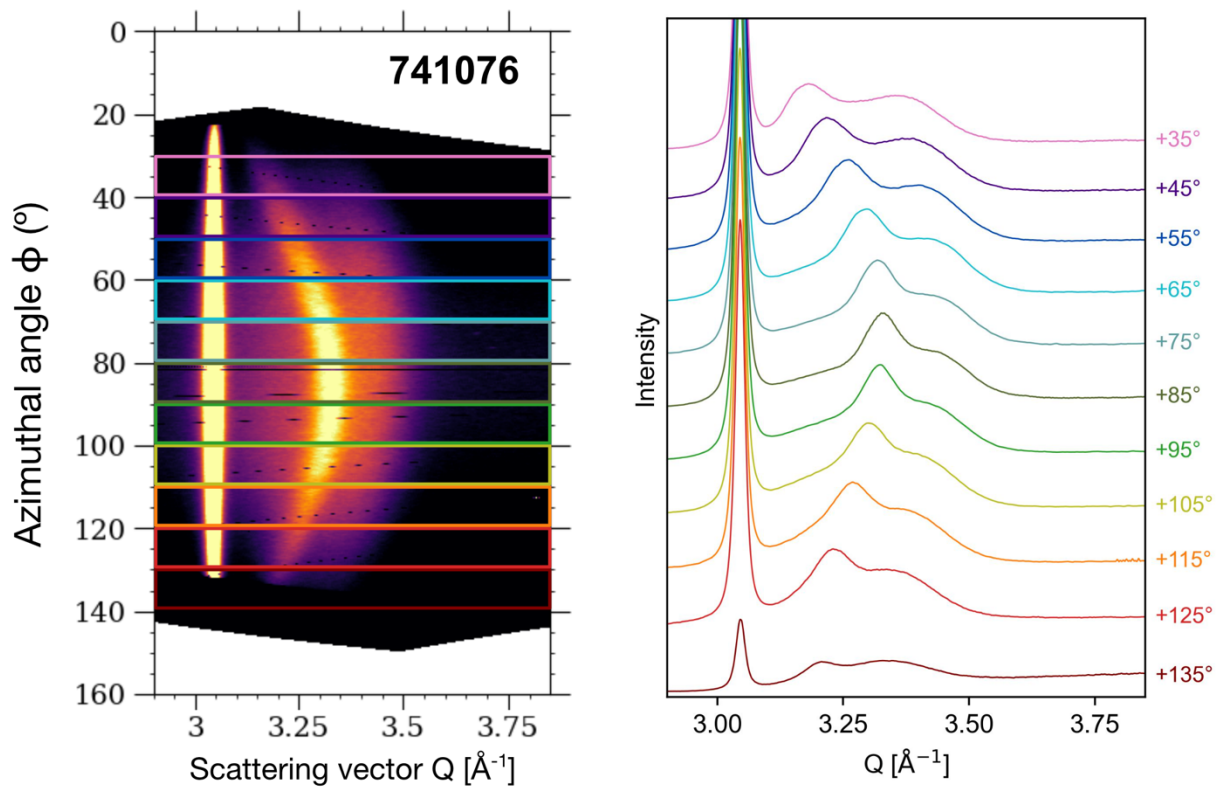
Extended Data Figure 7. Diffraction pattern of Run 1279187 (NPD shocked to 476 ± 10 GPa), with lineouts from each 10-degree azimuthal sector. To show the azimuthal variations more clearly, only diffraction from the $\{111\}$ planes is included.



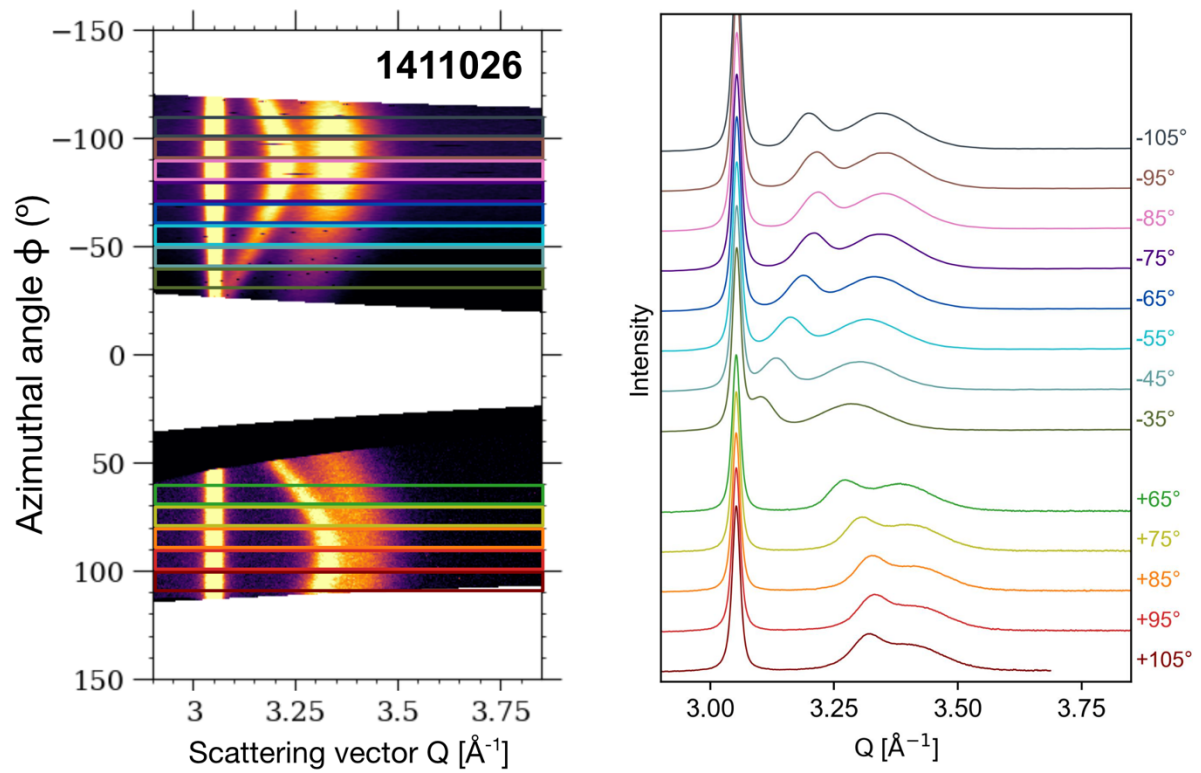
Extended Data Figure 8. Diffraction pattern of Run 741048 (NPD shocked to 425 ± 14 GPa), with lineouts from each 10-degree azimuthal sector. To show the azimuthal variations more clearly, only diffraction from the $\{111\}$ planes is included.



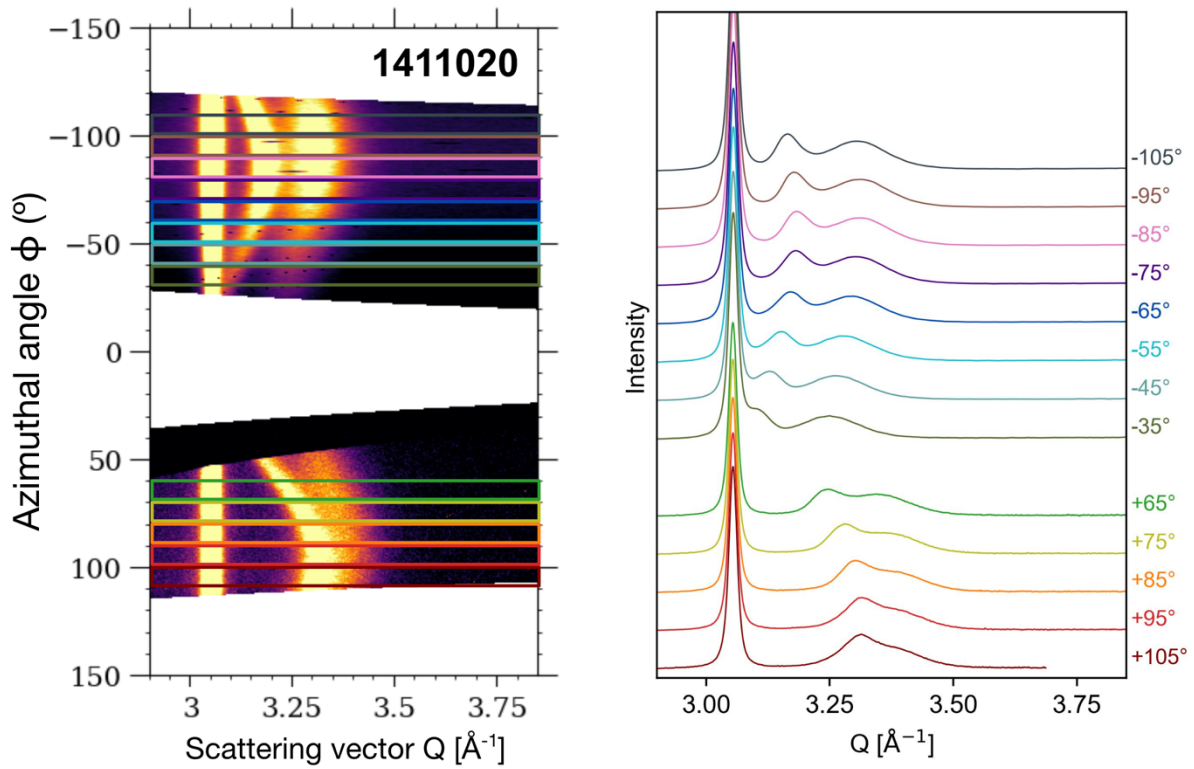
Extended Data Figure 9. Diffraction pattern of Run 1411016 (NPD shocked to 273 ± 9 GPa), with lineouts from each 10-degree azimuthal sector. To show the azimuthal variations more clearly, only diffraction from the $\{111\}$ planes is included.



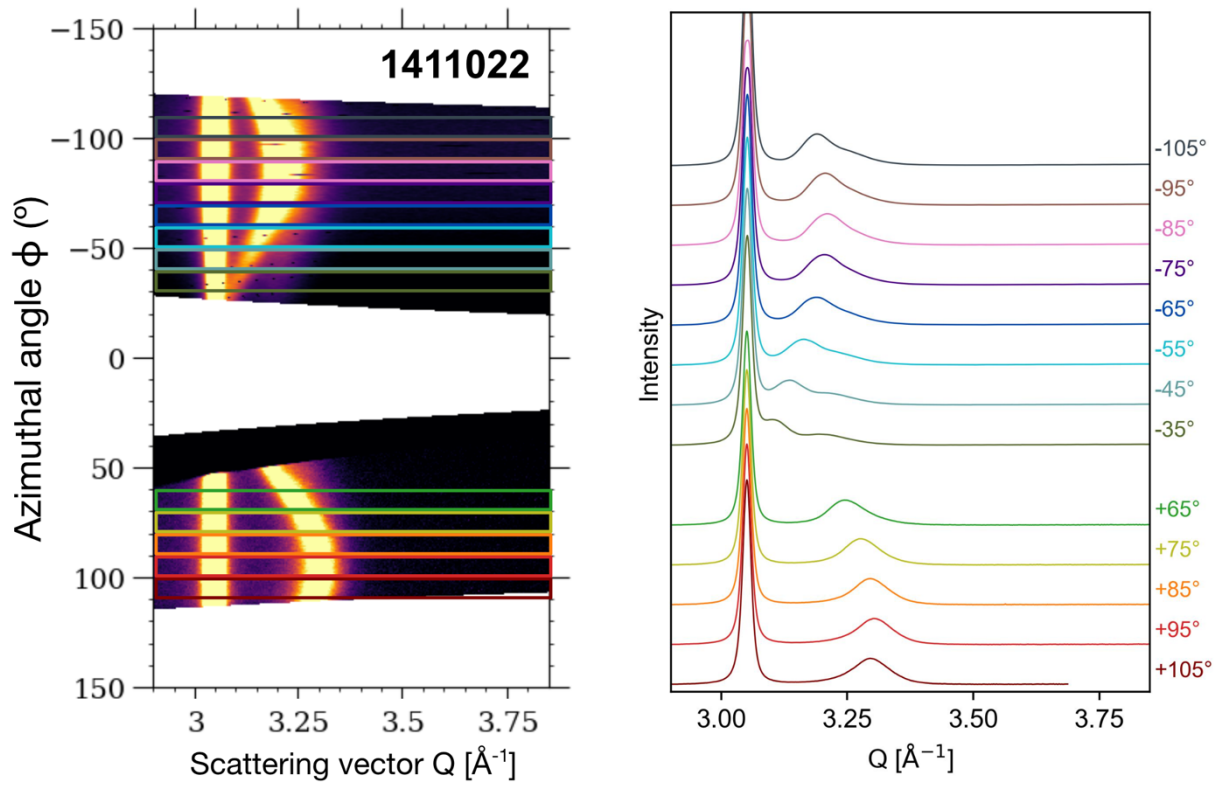
Extended Data Figure 10. Diffraction pattern of Run 741076 (NPD shocked to 227 ± 8 GPa), with lineouts from each 10-degree azimuthal sector. To show the azimuthal variations more clearly, only diffraction from the $\{111\}$ planes is included.



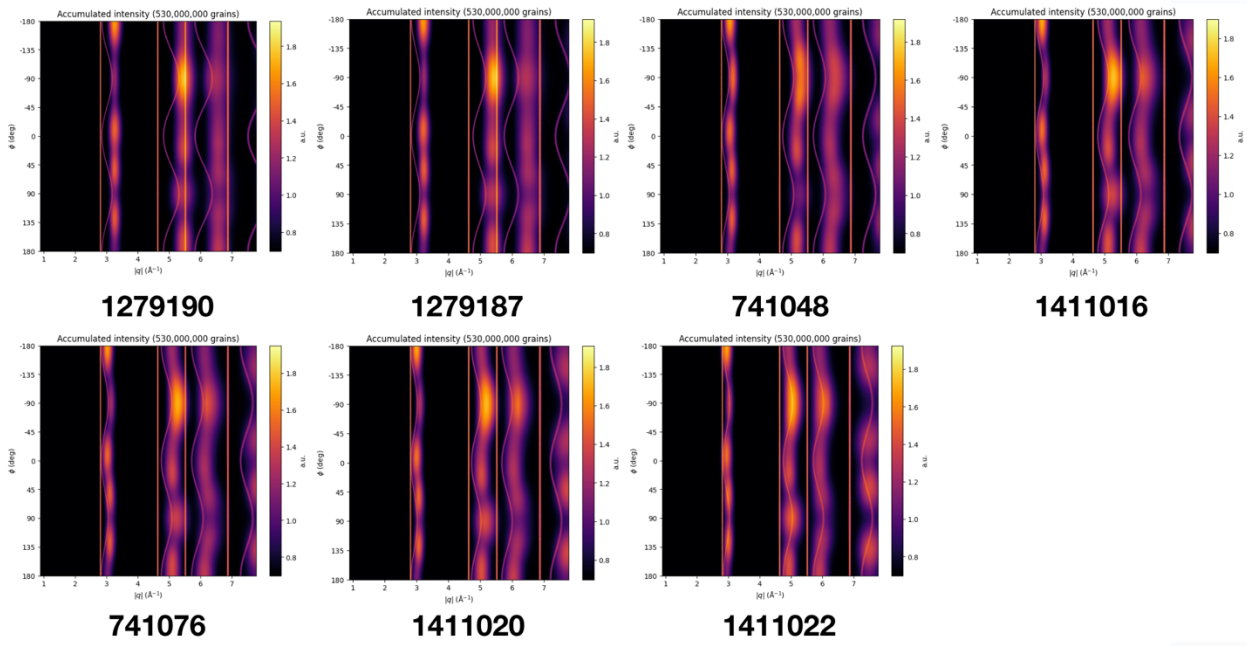
Extended Data Figure 11. Diffraction pattern of Run 1411026 (NPD shocked to 221 ± 8 GPa), with lineouts from each 10-degree azimuthal sector. To show the azimuthal variations more clearly, only diffraction from the $\{111\}$ planes is included.



Extended Data Figure 12. Diffraction pattern of Run 1411020 (NPD shocked to 181 ± 8 GPa), with lineouts from each 10-degree azimuthal sector. To show the azimuthal variations more clearly, only diffraction from the $\{111\}$ planes is included.



Extended Data Figure 13. Diffraction pattern of Run 1411022 (NPD shocked to 122 ± 12 GPa), with lineouts from each 10-degree azimuthal sector. To show the azimuthal variations more clearly, only diffraction from the $\{111\}$ planes is included.



Extended Data Figure 14. Diffraction simulations of $<110>$ fiber texture from forward model at different beam to shock angles, X-ray energies, and strain states, for direct comparison to each shock experiment. Run 741048 is not included as it is shown in Fig. 3 of the main text. A comparison of the corresponding simulation with each experimental diffraction pattern reveals that the patterns at shock stresses of 425 ± 14 GPa and above are consistent with $<110>$ fiber texture formation.

Shot ID	Beam to Shock (°)	E (keV)	$\varepsilon_{\parallel}^{\ell}$	$\varepsilon_{\perp}^{\ell}$	$\varepsilon_{\parallel}^p$	ε_{\perp}^p	$\varepsilon_{\parallel}^t$	ρ (g/cm ³)	σ_{\parallel} (GPa)	2τ (GPa)	P_M (GPa)
1279190	108	10.0	0.1402 ± 0.0010	0.1396 ± 0.0010	0.3116 ± 0.0059	-0.1396 ± 0.0010	0.452 ± 0.006	5.52 ± 0.02	565 ± 14	2 ± 6	564 ± 14
1279187	108	10.0	0.1347 ± 0.0006	0.1250 ± 0.0005	0.2770 ± 0.0030	-0.1250 ± 0.0005	0.412 ± 0.003	5.30 ± 0.01	476 ± 10	35 ± 3	452 ± 10
741048	110	10.0	0.1343 ± 0.0005	0.1141 ± 0.0023	0.2522 ± 0.0088	-0.1141 ± 0.0023	0.387 ± 0.009	5.17 ± 0.03	425 ± 14	69 ± 8	379 ± 15
1411016	115	12.0	0.1175 ± 0.0014	0.0815 ± 0.0010	0.1775 ± 0.0058	-0.0815 ± 0.0010	0.295 ± 0.006	4.72 ± 0.02	273 ± 9	93 ± 4	211 ± 9
741076	110	10.0	0.1133 ± 0.0005	0.0684 ± 0.0018	0.1487 ± 0.0059	-0.0684 ± 0.0018	0.262 ± 0.006	4.57 ± 0.02	227 ± 8	107 ± 5	156 ± 9
1411026	115	12.0	0.1118 ± 0.0016	0.0670 ± 0.0012	0.1455 ± 0.0065	-0.0670 ± 0.0012	0.257 ± 0.006	4.54 ± 0.02	221 ± 8	106 ± 5	151 ± 9
1411020	115	12.0	0.0993 ± 0.0020	0.0580 ± 0.0015	0.1248 ± 0.0077	-0.0580 ± 0.0015	0.224 ± 0.007	4.40 ± 0.03	181 ± 8	90 ± 6	121 ± 9
1411022	115	12.0	0.0761 ± 0.0030	0.0436 ± 0.0017	0.0922 ± 0.0101	-0.0436 ± 0.0017	0.168 ± 0.010	4.16 ± 0.03	122 ± 12	62 ± 7	82 ± 10

Extended Data Table 1. Table of experimental results. From left to right: Shot ID, angle from beam direction to shock direction, X-ray energy, longitudinal lattice strain, transverse lattice strain, longitudinal plastic strain, transverse plastic strain, uniaxial total strain, density, longitudinal stress, flow strength and mean pressure. All strains are given as compressive strain, i.e., positive values indicate compression while negative values indicate expansion.

σ_{\parallel} (GPa)	2τ (GPa)	P_M (GPa)	$\varepsilon_{\parallel}^t$	ρ (g/cm ³)	ρ_{partial} (m ⁻²)	ρ_{full} (m ⁻²)
623 ± 2	4 ± 1	620 ± 2	0.564 ± 0.003	5.96 ± 0.01	1.68×10^{16}	1.39×10^{17}
484 ± 3	20 ± 5	470 ± 5	0.486 ± 0.002	5.51 ± 0.01	2.30×10^{16}	1.25×10^{17}
366 ± 2	66 ± 7	322 ± 5	0.390 ± 0.006	5.01 ± 0.02	3.11×10^{16}	7.13×10^{16}
260 ± 4	87 ± 9	202 ± 7	0.290 ± 0.011	4.53 ± 0.03	3.26×10^{16}	3.02×10^{16}
227 ± 4	91 ± 8	167 ± 7	0.256 ± 0.012	4.38 ± 0.04	2.91×10^{16}	2.20×10^{16}
196 ± 5	90 ± 7	136 ± 7	0.223 ± 0.013	4.24 ± 0.04	1.59×10^{16}	1.15×10^{16}
167 ± 4	85 ± 5	110 ± 5	0.193 ± 0.010	4.11 ± 0.03	1.03×10^{16}	8.13×10^{15}
139 ± 2	79 ± 3	86 ± 3	0.161 ± 0.006	3.98 ± 0.02	2.80×10^{15}	2.84×10^{15}
108 ± 2	67 ± 1	63 ± 2	0.130 ± 0.002	3.86 ± 0.01	5.10×10^{14}	4.76×10^{14}

Extended Data Table 2. Table of MD simulation results. From left to right: longitudinal stress, flow strength, mean pressure, uniaxial total strain, density, a/6<112> partial dislocation density and a/2<110> full dislocation density. Dislocation densities are calculated for the grain interiors and are normalized to the proportion of cubic diamond atoms. Note that the starting density (ρ_0) in the MD simulations is 3.39 g/cm³, lower than that of the experiments. This is due to the smaller grain size (8 nm) used in the simulations, which causes a larger proportion of atoms incorporated in grain boundaries, which are less dense than the grain interiors.

Supplementary Material

Differences between experimental and MD results

Although our experimental and MD results show good agreement overall, there are a few differences in the results. The experiments show a sharper rise and fall in flow strength, and the NPD loses nearly all strength at a shock stress of 565 ± 8 GPa. By contrast, the simulations maintain significant strength of 20 ± 5 GPa even up to a shock stress of 484 GPa. Furthermore, the onset of texture formation in the experiments occurs at 425 ± 14 GPa, while in the MD simulations it occurs only at 623 GPa. We attribute these slight discrepancies to the differences in grain size and timescale between experiments and simulations. The MD simulations used a grain size of 8 nm and measured the shock response over several picoseconds, while experiments used 30-50 nm grains and measured ~ 1 ns after shock entry into the NPD. The smaller grain sizes of MD simulations may yield a slightly lower strength because the fraction of grain boundaries increases significantly compared to grain interiors, thereby lowering the shear modulus of the material [49].